Review | Vol. 8, No. 5 | 1 May 2017 | BIOMEDICAL OPTICS EXPRESS 2536

Biomedical Optics EXPRESS

Review of adaptive optics OCT (AO-OCT): principles and applications for retinal imaging [Invited]

MICHAEL PIRCHER[1,4] AND ROBERT J ZAWADZKI[2,3,5]

[1]*Medical University of Vienna, Center for Medical Physics and Biomedical Engineering, Währinger Gürtel 18-20/4L, 1090 Vienna, Austria*
[2]*UC Davis RISE Eye-Pod Laboratory, Dept. of Cell Biology and Human Anatomy, University of California Davis, 4320 Tupper Hall, Davis, CA 95616, USA*
[3]*Vision Science and Advanced Retinal Imaging Laboratory (VSRI) and Department of Ophthalmology and Vision Science, UC Davis, 4860 Y Street, Ste. 2400, Sacramento, CA 95817, USA*
[4]*michael.pircher@meduniwien.ac.at*
[5]*rjzawadzki@ucdavis.edu*

Abstract: In vivo imaging of the human retina with a resolution that allows visualization of cellular structures has proven to be essential to broaden our knowledge about the physiology of this precious and very complex neural tissue that enables the first steps in vision. Many pathologic changes originate from functional and structural alterations on a cellular scale, long before any degradation in vision can be noted. Therefore, it is important to investigate these tissues with a sufficient level of detail in order to better understand associated disease development or the effects of therapeutic intervention. Optical retinal imaging modalities rely on the optical elements of the eye itself (mainly the cornea and lens) to produce retinal images and are therefore affected by the specific arrangement of these elements and possible imperfections in curvature. Thus, aberrations are introduced to the imaging light and image quality is degraded. To compensate for these aberrations, adaptive optics (AO), a technology initially developed in astronomy, has been utilized. However, the axial sectioning provided by retinal AO-based fundus cameras and scanning laser ophthalmoscope instruments is limited to tens of micrometers because of the rather small available numerical aperture of the eye. To overcome this limitation and thus achieve much higher axial sectioning in the order of 2-5µm, AO has been combined with optical coherence tomography (OCT) into AO-OCT. This enabled for the first time in vivo volumetric retinal imaging with high isotropic resolution. This article summarizes the technical aspects of AO-OCT and provides an overview on its various implementations and some of its clinical applications. In addition, latest developments in the field, such as computational AO-OCT and wavefront sensor less AO-OCT, are covered.

OCIS codes: (170.4500) Optical coherence tomography; (170.4460) Ophthalmic optics and devices; (010.1080) Active or adaptive optics; (170.5755) Retina scanning; (330.5310) Vision - photoreceptors; (170.2655) Functional monitoring and imaging; (110.1758) Computational imaging.

References and links

1. D. Huang, E. A. Swanson, C. P. Lin, J. S. Schuman, W. G. Stinson, W. Chang, M. R. Hee, T. Flotte, K. Gregory, C. A. Puliafito, and J. G. Fujimoto, "Optical coherence tomography," Science **254**(5035), 1178–1181 (1991).
2. M. Wojtkowski, B. Kaluzny, and R. J. Zawadzki, "New directions in ophthalmic optical coherence tomography," Optom. Vis. Sci. **89**(5), 524–542 (2012).
3. T. E. de Carlo, A. Romano, N. K. Waheed, and J. S. Duker, "A review of optical coherence tomography angiography (OCTA)," Int J Retina Vitreous **1**(5), 5 (2015).
4. W. Drexler and J. G. Fujimoto, "State-of-the-art retinal optical coherence tomography," Prog. Retin. Eye Res. **27**(1), 45–88 (2008).
5. G. Walsh, W. N. Charman, and H. C. Howland, "Objective technique for the determination of monochromatic aberrations of the human eye," J. Opt. Soc. Am. A **1**(9), 987–992 (1984).
6. J. Liang and D. R. Williams, "Aberrations and retinal image quality of the normal human eye," J. Opt. Soc. Am. A **14**(11), 2873–2883 (1997).

#283959 https://doi.org/10.1364/BOE.8.002536
Journal © 2017 Received 3 Jan 2017; revised 8 Apr 2017; accepted 9 Apr 2017; published 19 Apr 2017

Biomedical Optics EXPRESS

7. Y. Zhang and A. Roorda, "Evaluating the lateral resolution of the adaptive optics scanning laser ophthalmoscope," J. Biomed. Opt. **11**(1), 014002 (2006).
8. L. N. Thibos, X. Hong, A. Bradley, and X. Cheng, "Statistical variation of aberration structure and image quality in a normal population of healthy eyes," J. Opt. Soc. Am. A **19**(12), 2329–2348 (2002).
9. J. Porter, A. Guirao, I. G. Cox, and D. R. Williams, "Monochromatic aberrations of the human eye in a large population," J. Opt. Soc. Am. A **18**(8), 1793–1803 (2001).
10. R. H. Webb and G. W. Hughes, "Scanning laser ophthalmoscope," IEEE Trans. Biomed. Eng. **28**(7), 488–492 (1981).
11. R. H. Webb, G. W. Hughes, and F. C. Delori, "Confocal scanning laser ophthalmoscope," Appl. Opt. **26**(8), 1492–1499 (1987).
12. M. Pircher, E. Götzinger, R. Leitgeb, A. F. Fercher, and C. K. Hitzenberger, "Speckle reduction in optical coherence tomography by frequency compounding," J. Biomed. Opt. **8**(3), 565–569 (2003).
13. D. L. Marks, T. S. Ralston, and S. A. Boppart, "Speckle reduction by I-divergence regularization in optical coherence tomography," J. Opt. Soc. Am. A **22**(11), 2366–2371 (2005).
14. M. Szkulmowski, I. Gorczynska, D. Szlag, M. Sylwestrzak, A. Kowalczyk, and M. Wojtkowski, "Efficient reduction of speckle noise in Optical Coherence Tomography," Opt. Express **20**(2), 1337–1359 (2012).
15. H. Babcock, "The possibility of compensating astronomical seeing," Publ. Astron. Soc. Pac. **65**(386), 229–236 (1953).
16. J. Liang, D. R. Williams, and D. T. Miller, "Supernormal vision and high-resolution retinal imaging through adaptive optics," J. Opt. Soc. Am. A **14**(11), 2884–2892 (1997).
17. A. Roorda, F. Romero-Borja, W. Donnelly Iii, H. Queener, T. Hebert, and M. Campbell, "Adaptive optics scanning laser ophthalmoscopy," Opt. Express **10**(9), 405–412 (2002).
18. B. Hermann, E. J. Fernández, A. Unterhuber, H. Sattmann, A. F. Fercher, W. Drexler, P. M. Prieto, and P. Artal, "Adaptive-optics ultrahigh-resolution optical coherence tomography," Opt. Lett. **29**(18), 2142–2144 (2004).
19. M. Pircher and R. Zawadzki, "Combining adaptive optics with optical coherence tomography: Unveiling the cellular structure of the human retina in vivo," Expert Rev. Ophthalmol. **2**(6), 1019 (2007).
20. D. T. Miller, O. P. Kocaoglu, Q. Wang, and S. Lee, "Adaptive optics and the eye (super resolution OCT)," Eye (Lond.) **25**(3), 321–330 (2011).
21. E. J. Fernandez and P. Artal, "Adaptive Optics in Ocular Optical Coherence Tomography," in *Optical Coherence Tomography*, R. Bernandes, and J. Cunha-Vaz, eds. (Springer, 2012), pp. 209–235.
22. R. J. Zawadzki and D. Miller, "Retinal AO OCT," in *Optical coherence tomography: Technology and Applications,* W. Drexler, and J. Fujimoto, eds. (Springer, 2015), pp. 1849–1920.
23. M. Pircher and C. K. Hitzenberger, "Acousto optic modulation based en-face AO SLO OCT," in *Optical Cohrence Tomography: Technology and Applications,* W. Drexler, and J. Fujimoto, eds. (Springer, 2015), pp. 1921–1939.
24. R. S. Jonnal, O. P. Kocaoglu, R. J. Zawadzki, Z. Liu, D. T. Miller, and J. S. Werner, "A Review of Adaptive Optics Optical Coherence Tomography: Technical Advances, Scientific Applications, and the Future," Invest. Ophthalmol. Vis. Sci. **57**(9), OCT51–OCT68 (2016).
25. A. N. S. Institute, "Amercian National Standard for Safe Use of Lasers," in *Z136.1* (Laser Institute of America, Orlando, FL, 2014).
26. I. E. C. (IEC), "Safety of laser products," in *Part 1: Equipment Classification and Requirements* (IEC-Central Office, 2014).
27. J. Liang, B. Grimm, S. Goelz, and J. F. Bille, "Objective measurement of wave aberrations of the human eye with the use of a Hartmann-Shack wave-front sensor," J. Opt. Soc. Am. A **11**(7), 1949–1957 (1994).
28. M. Laslandes, M. Salas, C. K. Hitzenberger, and M. Pircher, "Influence of wave-front sampling in adaptive optics retinal imaging," Biomed. Opt. Express **8**(2), 1083–1100 (2017).
29. S. Tuohy and A. G. Podoleanu, "Depth-resolved wavefront aberrations using a coherence-gated Shack-Hartmann wavefront sensor," Opt. Express **18**(4), 3458–3476 (2010).
30. J. Wang, J. F. Léger, J. Binding, A. C. Boccara, S. Gigan, and L. Bourdieu, "Measuring aberrations in the rat brain by coherence-gated wavefront sensing using a Linnik interferometer," Biomed. Opt. Express **3**(10), 2510–2525 (2012).
31. Y. Zhang, J. Rha, R. Jonnal, and D. Miller, "Adaptive optics parallel spectral domain optical coherence tomography for imaging the living retina," Opt. Express **13**(12), 4792–4811 (2005).
32. R. J. Zawadzki, S. M. Jones, S. S. Olivier, M. Zhao, B. A. Bower, J. A. Izatt, S. Choi, S. Laut, and J. S. Werner, "Adaptive-optics optical coherence tomography for high-resolution and high-speed 3D retinal in vivo imaging," Opt. Express **13**(21), 8532–8546 (2005).
33. D. Merino, C. Dainty, A. Bradu, and A. G. Podoleanu, "Adaptive optics enhanced simultaneous en-face optical coherence tomography and scanning laser ophthalmoscopy," Opt. Express **14**(8), 3345–3353 (2006).
34. C. E. Bigelow, N. V. Iftimia, R. D. Ferguson, T. E. Ustun, B. Bloom, and D. X. Hammer, "Compact multimodal adaptive-optics spectral-domain optical coherence tomography instrument for retinal imaging," J. Opt. Soc. Am. A **24**(5), 1327–1336 (2007).
35. E. J. Fernández, B. Hermann, B. Povazay, A. Unterhuber, H. Sattmann, B. Hofer, P. K. Ahnelt, and W. Drexler, "Ultrahigh resolution optical coherence tomography and pancorrection for cellular imaging of the living human retina," Opt. Express **16**(15), 11083–11094 (2008).

Biomedical Optics EXPRESS

36. E. J. Fernández, B. Povazay, B. Hermann, A. Unterhuber, H. Sattmann, P. M. Prieto, R. Leitgeb, P. Ahnelt, P. Artal, and W. Drexler, "Three-dimensional adaptive optics ultrahigh-resolution optical coherence tomography using a liquid crystal spatial light modulator," Vision Res. **45**(28), 3432–3444 (2005).
37. Y. Jian, R. J. Zawadzki, and M. V. Sarunic, "Adaptive optics optical coherence tomography for in vivo mouse retinal imaging," J. Biomed. Opt. **18**(5), 056007 (2013).
38. Y. Jian, J. Xu, M. A. Gradowski, S. Bonora, R. J. Zawadzki, and M. V. Sarunic, "Wavefront sensorless adaptive optics optical coherence tomography for in vivo retinal imaging in mice," Biomed. Opt. Express **5**(2), 547–559 (2014).
39. R. J. Zawadzki, S. S. Choi, S. M. Jones, S. S. Oliver, and J. S. Werner, "Adaptive optics-optical coherence tomography: optimizing visualization of microscopic retinal structures in three dimensions," J. Opt. Soc. Am. A **24**(5), 1373–1383 (2007).
40. D. X. Hammer, R. D. Ferguson, M. Mujat, A. Patel, E. Plumb, N. Iftimia, T. Y. P. Chui, J. D. Akula, and A. B. Fulton, "Multimodal adaptive optics retinal imager: design and performance," J. Opt. Soc. Am. A **29**(12), 2598–2607 (2012).
41. N. Doble, D. T. Miller, G. Yoon, and D. R. Williams, "Requirements for discrete actuator and segmented wavefront correctors for aberration compensation in two large populations of human eyes," Appl. Opt. **46**(20), 4501–4514 (2007).
42. F. Felberer, J. S. Kroisamer, B. Baumann, S. Zotter, U. Schmidt-Erfurth, C. K. Hitzenberger, and M. Pircher, "Adaptive optics SLO/OCT for 3D imaging of human photoreceptors in vivo," Biomed. Opt. Express **5**(2), 439–456 (2014).
43. H. Hofer, P. Artal, B. Singer, J. L. Aragón, and D. R. Williams, "Dynamics of the eye's wave aberration," J. Opt. Soc. Am. A **18**(3), 497–506 (2001).
44. H. Hofer, L. Chen, G. Y. Yoon, B. Singer, Y. Yamauchi, and D. R. Williams, "Improvement in retinal image quality with dynamic correction of the eye's aberrations," Opt. Express **8**(11), 631–643 (2001).
45. E. Logean, E. Dalimier, and C. Dainty, "Measured double-pass intensity point-spread function after adaptive optics correction of ocular aberrations," Opt. Express **16**(22), 17348–17357 (2008).
46. A. Marechal, "Etude des effets combines de la diffraction et des aberrations geometriques sur l'image d'un point lumineux," Revue d'Optique **26** (1947).
47. Y. Jian, S. Lee, M. J. Ju, M. Heisler, W. Ding, R. J. Zawadzki, S. Bonora, and M. V. Sarunic, "Lens-based wavefront sensorless adaptive optics swept source OCT," Sci. Rep. **6**(1), 27620 (2016).
48. S. Bonora and R. J. Zawadzki, "Wavefront sensorless modal deformable mirror correction in adaptive optics: optical coherence tomography," Opt. Lett. **38**(22), 4801–4804 (2013).
49. Y. Jian, J. Xu, M. A. Gradowski, S. Bonora, R. J. Zawadzki, and M. V. Sarunic, "Wavefront sensorless adaptive optics optical coherence tomography for in vivo retinal imaging in mice," Biomed. Opt. Express **5**(2), 547–559 (2014).
50. K. S. Wong, Y. Jian, M. Cua, S. Bonora, R. J. Zawadzki, and M. V. Sarunic, "In vivo imaging of human photoreceptor mosaic with wavefront sensorless adaptive optics optical coherence tomography," Biomed. Opt. Express **6**(2), 580–590 (2015).
51. P. Xiao, M. Fink, and A. C. Boccara, "Adaptive optics full-field optical coherence tomography," J. Biomed. Opt. **21**(12), 121505 (2016).
52. S. Bonora, Y. Jian, P. Zhang, A. Zam, E. N. Pugh, Jr., R. J. Zawadzki, and M. V. Sarunic, "Wavefront correction and high-resolution in vivo OCT imaging with an objective integrated multi-actuator adaptive lens," Opt. Express **23**(17), 21931–21941 (2015).
53. F. Felberer, J. S. Kroisamer, C. K. Hitzenberger, and M. Pircher, "Lens based adaptive optics scanning laser ophthalmoscope," Opt. Express **20**(16), 17297–17310 (2012).
54. H. R. G. W. Verstraete, S. Wahls, J. Kalkman, and M. Verhaegen, "Model-based sensor-less wavefront aberration correction in optical coherence tomography," Opt. Lett. **40**(24), 5722–5725 (2015).
55. H. R. G. W. Verstraete, M. Heisler, M. J. Ju, D. Wahl, L. Bliek, J. Kalkman, S. Bonora, Y. Jian, M. Verhaegen, and M. V. Sarunic, "Wavefront sensorless adaptive optics OCT with the DONE algorithm for in vivo human retinal imaging," Biomed. Opt. Express **8**(4), 2261–2275 (2017).
56. J. Polans, B. Keller, O. M. Carrasco-Zevallos, F. LaRocca, E. Cole, H. E. Whitson, E. M. Lad, S. Farsiu, and J. A. Izatt, "Wide-field retinal optical coherence tomography with wavefront sensorless adaptive optics for enhanced imaging of targeted regions," Biomed. Opt. Express **8**(1), 16–37 (2017).
57. M. Reddikumar, A. Tanabe, N. Hashimoto, and B. Cense, "Optical coherence tomography with a 2.8-mm beam diameter and sensorless defocus and astigmatism correction," J. Biomed. Opt. **22**(2), 026005 (2017).
58. A. Kumar, T. Kamali, R. Platzer, A. Unterhuber, W. Drexler, and R. A. Leitgeb, "Anisotropic aberration correction using region of interest based digital adaptive optics in Fourier domain OCT," Biomed. Opt. Express **6**(4), 1124–1134 (2015).
59. P. Pande, Y. Z. Liu, F. A. South, and S. A. Boppart, "Automated computational aberration correction method for broadband interferometric imaging techniques," Opt. Lett. **41**(14), 3324–3327 (2016).
60. N. D. Shemonski, F. A. South, Y. Z. Liu, S. G. Adie, P. S. Carney, and S. A. Boppart, "Computational high-resolution optical imaging of the living human retina," Nat. Photonics **9**(7), 440–443 (2015).
61. Y. Xu, Y. Z. Liu, S. A. Boppart, and P. S. Carney, "Automated interferometric synthetic aperture microscopy and computational adaptive optics for improved optical coherence tomography," Appl. Opt. **55**(8), 2034–2041 (2016).

Biomedical Optics EXPRESS

62. D. Hillmann, H. Spahr, C. Hain, H. Sudkamp, G. Franke, C. Pfaffle, C. Winter, and G. Huttmann, "Aberration-free volumetric high-speed imaging of in vivo retina," Sci. Rep. **6**, 35209 (2016).
63. P. Xiao, M. Fink, and A. C. Boccara, "Full-field spatially incoherent illumination interferometry: a spatial resolution almost insensitive to aberrations," Opt. Lett. **41**(17), 3920–3923 (2016).
64. A. F. Fercher, "Optical coherence tomography - development, principles, applications," Z. Med. Phys. **20**(4), 251–276 (2010).
65. C. K. Hitzenberger, A. Baumgartner, W. Drexler, and A. F. Fercher, "Dispersion effects in partial coherence interferometry: implications for intraocular ranging," J. Biomed. Opt. **4**(1), 144–151 (1999).
66. R. H. Webb, "Confocal optical microscopy," Rep. Prog. Phys. **59**(3), 427–471 (1996).
67. J. A. Izatt, M. A. Choma, and A. Dhalla, "Theory of optical coherence tomography," in *Optical coherence tomography*, W. Drexler, and J. G. Fujimoto, eds. (Springer, 2015).
68. T. Wilson 1 and A. R. Carlini, "Size of the detector in confocal imaging systems," Opt. Lett. **12**(4), 227–229 (1987).
69. T. Dabbs and M. Glass, "Fiber-Optic Confocal Microscope: FOCON," Appl. Opt. **31**(16), 3030–3035 (1992).
70. M. Gu, C. J. R. Sheppard, and X. Gan, "Image-formation in a fiberoptic confocal scanning microscope," J. Opt. Soc. Am. A **8**(11), 1755–1761 (1991).
71. J. Holmes, S. Hattersley, N. Stone, F. Bazant-Hegemark, and H. Barr, "Multi-channel Fourier Domain OCT system with superior lateral resolution for biomedical applications," P. Soc. Photo-Op. Ins. **6847**, O8470 (2008).
72. R. A. Leitgeb, M. Villiger, A. H. Bachmann, L. Steinmann, and T. Lasser, "Extended focus depth for Fourier domain optical coherence microscopy," Opt. Lett. **31**(16), 2450–2452 (2006).
73. R. E. Bedford and G. Wyszecki, "Axial chromatic aberration of the human eye," J. Opt. Soc. Am. **47**(6), 564–565 (1957).
74. P. Simonet and M. C. W. Campbell, "The optical transverse chromatic aberration on the fovea of the human eye," Vision Res. **30**(2), 187–206 (1990).
75. E. Fernández, A. Unterhuber, P. Prieto, B. Hermann, W. Drexler, and P. Artal, "Ocular aberrations as a function of wavelength in the near infrared measured with a femtosecond laser," Opt. Express **13**(2), 400–409 (2005).
76. R. J. Zawadzki, B. Cense, Y. Zhang, S. S. Choi, D. T. Miller, and J. S. Werner, "Ultrahigh-resolution optical coherence tomography with monochromatic and chromatic aberration correction," Opt. Express **16**(11), 8126–8143 (2008).
77. W. M. Harmening, P. Tiruveedhula, A. Roorda, and L. C. Sincich, "Measurement and correction of transverse chromatic offsets for multi-wavelength retinal microscopy in the living eye," Biomed. Opt. Express **3**(9), 2066–2077 (2012).
78. P. Bedggood, M. Daaboul, R. Ashman, G. Smith, and A. Metha, "Characteristics of the human isoplanatic patch and implications for adaptive optics retinal imaging," J. Biomed. Opt. **13**(2), 024008 (2008).
79. J. Thaung, P. Knutsson, Z. Popovic, and M. Owner-Petersen, "Dual-conjugate adaptive optics for wide-field high-resolution retinal imaging," Opt. Express **17**(6), 4454–4467 (2009).
80. C. R. Vogel, D. W. Arathorn, A. Roorda, and A. Parker, "Retinal motion estimation in adaptive optics scanning laser ophthalmoscopy," Opt. Express **14**(2), 487–497 (2006).
81. T. Klein, W. Wieser, C. M. Eigenwillig, B. R. Biedermann, and R. Huber, "Megahertz OCT for ultrawide-field retinal imaging with a 1050 nm Fourier domain mode-locked laser," Opt. Express **19**(4), 3044–3062 (2011).
82. O. P. Kocaoglu, T. L. Turner, Z. Liu, and D. T. Miller, "Adaptive optics optical coherence tomography at 1 MHz," Biomed. Opt. Express **5**(12), 4186–4200 (2014).
83. O. P. Kocaoglu, S. Lee, R. S. Jonnal, Q. Wang, A. E. Herde, J. C. Derby, W. Gao, and D. T. Miller, "Imaging cone photoreceptors in three dimensions and in time using ultrahigh resolution optical coherence tomography with adaptive optics," Biomed. Opt. Express **2**(4), 748–763 (2011).
84. R. J. Zawadzki, S. M. Jones, S. Pilli, S. Balderas-Mata, D. Y. Kim, S. S. Olivier, and J. S. Werner, "Integrated adaptive optics optical coherence tomography and adaptive optics scanning laser ophthalmoscope system for simultaneous cellular resolution in vivo retinal imaging," Biomed. Opt. Express **2**(6), 1674–1686 (2011).
85. O. P. Kocaoglu, R. D. Ferguson, R. S. Jonnal, Z. Liu, Q. Wang, D. X. Hammer, and D. T. Miller, "Adaptive optics optical coherence tomography with dynamic retinal tracking," Biomed. Opt. Express **5**(7), 2262–2284 (2014).
86. R. S. Jonnal, J. Qu, K. Thorn, and D. T. Miller, "En-face coherence gating of the retina with adaptive optics," Invest. Ophthalmol. Vis. Sci. **44**, U275 (2003).
87. J. F. de Boer, B. Cense, B. H. Park, M. C. Pierce, G. J. Tearney, and B. E. Bouma, "Improved signal-to-noise ratio in spectral-domain compared with time-domain optical coherence tomography," Opt. Lett. **28**(21), 2067–2069 (2003).
88. R. Leitgeb, C. Hitzenberger, and A. Fercher, "Performance of fourier domain vs. time domain optical coherence tomography," Opt. Express **11**(8), 889–894 (2003).
89. M. Choma, M. Sarunic, C. Yang, and J. Izatt, "Sensitivity advantage of swept source and Fourier domain optical coherence tomography," Opt. Express **11**(18), 2183–2189 (2003).
90. R. S. Jonnal, O. P. Kocaoglu, R. J. Zawadzki, S. H. Lee, J. S. Werner, and D. T. Miller, "The Cellular Origins of the Outer Retinal Bands in Optical Coherence Tomography Images," Invest. Ophthalmol. Vis. Sci. **55**(12), 7904–7918 (2014).
91. A. G. Podoleanu, G. M. Dobre, D. J. Webb, and D. A. Jackson, "Coherence imaging by use of a Newton rings sampling function," Opt. Lett. **21**(21), 1789–1791 (1996).

Biomedical Optics EXPRESS

92. M. Pircher, R. J. Zawadzki, J. W. Evans, J. S. Werner, and C. K. Hitzenberger, "Simultaneous imaging of human cone mosaic with adaptive optics enhanced scanning laser ophthalmoscopy and high-speed transversal scanning optical coherence tomography," Opt. Lett. **33**(1), 22–24 (2008).
93. M. Pircher, E. Götzinger, and C. K. Hitzenberger, "Dynamic focus in optical coherence tomography for retinal imaging," J. Biomed. Opt. **11**(5), 054013 (2006).
94. M. Pircher, E. Götzinger, H. Sattmann, R. A. Leitgeb, and C. K. Hitzenberger, "In vivo investigation of human cone photoreceptors with SLO/OCT in combination with 3D motion correction on a cellular level," Opt. Express **18**(13), 13935–13944 (2010).
95. M. Pircher, B. Baumann, E. Götzinger, H. Sattmann, and C. K. Hitzenberger, "Simultaneous SLO/OCT imaging of the human retina with axial eye motion correction," Opt. Express **15**(25), 16922–16932 (2007).
96. A. Dubra and Y. Sulai, "Reflective afocal broadband adaptive optics scanning ophthalmoscope," Biomed. Opt. Express **2**(6), 1757–1768 (2011).
97. Y. Zhang, B. Cense, J. Rha, R. S. Jonnal, W. Gao, R. J. Zawadzki, J. S. Werner, S. Jones, S. Olivier, and D. T. Miller, "High-speed volumetric imaging of cone photoreceptors with adaptive optics spectral-domain optical coherence tomography," Opt. Express **14**(10), 4380–4394 (2006).
98. R. S. Jonnal, O. P. Kocaoglu, Q. Wang, S. Lee, and D. T. Miller, "Phase-sensitive imaging of the outer retina using optical coherence tomography and adaptive optics," Biomed. Opt. Express **3**(1), 104–124 (2012).
99. S. H. Lee, J. S. Werner, and R. J. Zawadzki, "Improved visualization of outer retinal morphology with aberration cancelling reflective optical design for adaptive optics - optical coherence tomography," Biomed. Opt. Express **4**(11), 2508–2517 (2013).
100. A. Meadway, X. Wang, C. A. Curcio, and Y. Zhang, "Microstructure of subretinal drusenoid deposits revealed by adaptive optics imaging," Biomed. Opt. Express **5**(3), 713–727 (2014).
101. C. Torti, B. Povazay, B. Hofer, A. Unterhuber, J. Carroll, P. K. Ahnelt, and W. Drexler, "Adaptive optics optical coherence tomography at 120,000 depth scans/s for non-invasive cellular phenotyping of the living human retina," Opt. Express **17**(22), 19382–19400 (2009).
102. B. Povazay, K. Bizheva, B. Hermann, A. Unterhuber, H. Sattmann, A. Fercher, W. Drexler, C. Schubert, P. Ahnelt, M. Mei, R. Holzwarth, W. Wadsworth, J. Knight, and P. S. Russell, "Enhanced visualization of choroidal vessels using ultrahigh resolution ophthalmic OCT at 1050 nm," Opt. Express **11**(17), 1980–1986 (2003).
103. E. C. W. Lee, J. F. de Boer, M. Mujat, H. Lim, and S. H. Yun, "In vivo optical frequency domain imaging of human retina and choroid," Opt. Express **14**(10), 4403–4411 (2006).
104. K. Kurokawa, K. Sasaki, S. Makita, M. Yamanari, B. Cense, and Y. Yasuno, "Simultaneous high-resolution retinal imaging and high-penetration choroidal imaging by one-micrometer adaptive optics optical coherence tomography," Opt. Express **18**(8), 8515–8527 (2010).
105. M. Mujat, R. D. Ferguson, A. H. Patel, N. Iftimia, N. Lue, and D. X. Hammer, "High resolution multimodal clinical ophthalmic imaging system," Opt. Express **18**(11), 11607–11621 (2010).
106. K. Kurokawa, K. Sasaki, S. Makita, Y. J. Hong, and Y. Yasuno, "Three-dimensional retinal and choroidal capillary imaging by power Doppler optical coherence angiography with adaptive optics," Opt. Express **20**(20), 22796–22812 (2012).
107. Z. Wang, B. Potsaid, L. Chen, C. Doerr, H. C. Lee, T. Nielson, V. Jayaraman, A. E. Cable, E. Swanson, and J. G. Fujimoto, "Cubic meter volume optical coherence tomography," Optica **3**(12), 1496–1503 (2016).
108. Y. Jian, S. Lee, M. J. Ju, M. Heisler, W. Ding, R. J. Zawadzki, S. Bonora, and M. V. Sarunic, "Lens-based wavefront sensorless adaptive optics swept source OCT," Sci. Rep. **6**(1), 27620 (2016).
109. A. W. Snyder and C. Pask, "The Stiles-Crawford effect--explanation and consequences," Vision Res. **13**(6), 1115–1137 (1973).
110. W. Gao, B. Cense, Y. Zhang, R. S. Jonnal, and D. T. Miller, "Measuring retinal contributions to the optical Stiles-Crawford effect with optical coherence tomography," Opt. Express **16**(9), 6486–6501 (2008).
111. Z. Liu, O. P. Kocaoglu, and D. T. Miller, "3D imaging of retinal pigment epithelial cells in the living human retina," Invest. Ophthalmol. Vis. Sci. **57**(9), OCT533 (2016).
112. Z. Liu, O. P. Kocaoglu, T. L. Turner, and D. T. Miller, "Modal content of living human cone photoreceptors," Biomed. Opt. Express **6**(9), 3378–3404 (2015).
113. C. A. Curcio, K. R. Sloan, R. E. Kalina, and A. E. Hendrickson, "Human photoreceptor topography," J. Comp. Neurol. **292**(4), 497–523 (1990).
114. V. J. Srinivasan, B. K. Monson, M. Wojtkowski, R. A. Bilonick, I. Gorczynska, R. Chen, J. S. Duker, J. S. Schuman, and J. G. Fujimoto, "Characterization of outer retinal morphology with high-speed, ultrahigh-resolution optical coherence tomography," Invest. Ophthalmol. Vis. Sci. **49**(4), 1571–1579 (2008).
115. M. Pircher, B. Baumann, H. Sattman, E. Götzinger, and C. K. Hitzenberger, "High speed, high resolution SLO/OCT for investigating temporal changes of single cone photoreceptors in vivo " in *ECBO 2009*, P. E. Andersen, and B. Bouma, eds. (SPIE, Munich, 2009).
116. M. Pircher, J. S. Kroisamer, F. Felberer, H. Sattmann, E. Götzinger, and C. K. Hitzenberger, "Temporal changes of human cone photoreceptors observed in vivo with SLO/OCT," Biomed. Opt. Express **2**(1), 100–112 (2011).
117. R. S. Jonnal, J. R. Besecker, J. C. Derby, O. P. Kocaoglu, B. Cense, W. Gao, Q. Wang, and D. T. Miller, "Imaging outer segment renewal in living human cone photoreceptors," Opt. Express **18**(5), 5257–5270 (2010).
118. O. P. Kocaoglu, Z. Liu, F. Zhang, K. Kurokawa, R. S. Jonnal, and D. T. Miller, "Photoreceptor disc shedding in the living human eye," Biomed. Opt. Express **7**(11), 4554–4568 (2016).

Biomedical Optics EXPRESS

119. D. Hillmann, H. Spahr, C. Pfäffle, H. Sudkamp, G. Franke, and G. Hüttmann, "In vivo optical imaging of physiological responses to photostimulation in human photoreceptors," Proc. Natl. Acad. Sci. U.S.A. **113**(46), 13138–13143 (2016).
120. P. Zhang, R. J. Zawadzki, M. Goswami, P. T. Nguyen, V. Yarov-Yarovoy, M. E. Burns, and E. N. Pugh, Jr., "In vivo optophysiology reveals that G-protein activation triggers osmotic swelling and increased light scattering of rod photoreceptors," Proc. Natl. Acad. Sci. U.S.A. **114**(14), E2937–E2946 (2017).
121. O. P. Kocaoglu, B. Cense, R. S. Jonnal, Q. Wang, S. Lee, W. Gao, and D. T. Miller, "Imaging retinal nerve fiber bundles using optical coherence tomography with adaptive optics," Vision Res. **51**(16), 1835–1844 (2011).
122. Q. Wang, O. P. Kocaoglu, B. Cense, J. Bruestle, R. S. Jonnal, W. Gao, and D. T. Miller, "Imaging retinal capillaries using ultrahigh-resolution optical coherence tomography and adaptive optics," Invest. Ophthalmol. Vis. Sci. **52**(9), 6292–6299 (2011).
123. F. Felberer, M. Rechenmacher, R. Haindl, B. Baumann, C. K. Hitzenberger, and M. Pircher, "Imaging of retinal vasculature using adaptive optics SLO/OCT," Biomed. Opt. Express **6**(4), 1407–1418 (2015).
124. I. Gorczynska, J. V. Migacz, R. J. Zawadzki, A. G. Capps, and J. S. Werner, "Comparison of amplitude-decorrelation, speckle-variance and phase-variance OCT angiography methods for imaging the human retina and choroid," Biomed. Opt. Express **7**(3), 911–942 (2016).
125. R. F. Spaide, J. G. Fujimoto, and N. K. Waheed, "Image artifacts in optical coherence tomography angiography," Retina **35**(11), 2163–2180 (2015).
126. M. Salas, M. Augustin, L. Ginner, A. Kumar, B. Baumann, R. Leitgeb, W. Drexler, S. Prager, J. Hafner, U. Schmidt-Erfurth, and M. Pircher, "Visualization of micro-capillaries using optical coherence tomography angiography with and without adaptive optics," Biomed. Opt. Express **8**(1), 207–222 (2017).
127. E. Götzinger, M. Pircher, B. Baumann, T. Schmoll, H. Sattmann, R. A. Leitgeb, and C. K. Hitzenberger, "Speckle noise reduction in high speed polarization sensitive spectral domain optical coherence tomography," Opt. Express **19**(15), 14568–14585 (2011).
128. B. Cense, W. Gao, J. M. Brown, S. M. Jones, R. S. Jonnal, M. Mujat, B. H. Park, J. F. de Boer, and D. T. Miller, "Retinal imaging with polarization-sensitive optical coherence tomography and adaptive optics," Opt. Express **17**(24), 21634–21651 (2009).
129. A. Panorgias, R. J. Zawadzki, A. G. Capps, A. A. Hunter, L. S. Morse, and J. S. Werner, "Multimodal assessment of microscopic morphology and retinal function in patients with geographic atrophy," Invest. Ophthalmol. Vis. Sci. **54**(6), 4372–4384 (2013).
130. X. Zhang, J. B. Saaddine, C. F. Chou, M. F. Cotch, Y. J. Cheng, L. S. Geiss, E. W. Gregg, A. L. Albright, B. E. K. Klein, and R. Klein, "Prevalence of Diabetic Retinopathy in the United States, 2005-2008," JAMA **304**(6), 649–656 (2010).
131. S. S. Choi, R. J. Zawadzki, M. C. Lim, J. D. Brandt, J. L. Keltner, N. Doble, and J. S. Werner, "Evidence of outer retinal changes in glaucoma patients as revealed by ultrahigh-resolution in vivo retinal imaging," Br. J. Ophthalmol. **95**(1), 131–141 (2011).
132. J. S. Werner, J. L. Keltner, R. J. Zawadzki, and S. S. Choi, "Outer retinal abnormalities associated with inner retinal pathology in nonglaucomatous and glaucomatous optic neuropathies," Eye (Lond.) **25**(3), 279–289 (2011).
133. Z. M. Dong, G. Wollstein, B. Wang, and J. S. Schuman, "Adaptive optics optical coherence tomography in glaucoma," Prog. Retin. Eye Res. **57**, 76–88 (2017).
134. S. S. Park, G. Bauer, M. Abedi, S. Pontow, A. Panorgias, R. Jonnal, R. J. Zawadzki, J. S. Werner, and J. Nolta, "Intravitreal Autologous Bone Marrow CD^{34+} Cell Therapy for Ischemic and Degenerative Retinal Disorders: Preliminary Phase 1 Clinical Trial Findings," Invest. Ophthalmol. Vis. Sci. **56**(1), 81–89 (2014).
135. D. X. Hammer, N. V. Iftimia, R. D. Ferguson, C. E. Bigelow, T. E. Ustun, A. M. Barnaby, and A. B. Fulton, "Foveal fine structure in retinopathy of prematurity: an adaptive optics Fourier domain optical coherence tomography study," Invest. Ophthalmol. Vis. Sci. **49**(5), 2061–2070 (2008).
136. B. Považay, B. Hofer, C. Torti, B. Hermann, A. R. Tumlinson, M. Esmaeelpour, C. A. Egan, A. C. Bird, and W. Drexler, "Impact of enhanced resolution, speed and penetration on three-dimensional retinal optical coherence tomography," Opt. Express **17**(5), 4134–4150 (2009).
137. L. T. Labriola, A. D. Legarreta, J. E. Legarreta, Z. Nadler, D. Gallagher, D. X. Hammer, R. D. Ferguson, N. Iftimia, G. Wollstein, and J. S. Schuman, "Imaging with multimodal adaptive optics optical coherence tomography in multiple evanescent white dot syndrome: The structure and functional relationship," Retin. Cases Brief Rep. **10**(4), 302–309 (2016).
138. M. Salas, W. Drexler, X. Levecq, B. Lamory, M. Ritter, S. Prager, J. Hafner, U. Schmidt-Erfurth, and M. Pircher, "Multi-modal adaptive optics system including fundus photography and optical coherence tomography for the clinical setting," Biomed. Opt. Express **7**(5), 1783–1796 (2016).
139. D. T. Miller, D. R. Williams, G. M. Morris, and J. Liang, "Images of cone photoreceptors in the living human eye," Vision Res. **36**(8), 1067–1079 (1996).
140. M. Pircher, B. Baumann, E. Götzinger, and C. K. Hitzenberger, "Retinal cone mosaic imaged with transverse scanning optical coherence tomography," Opt. Lett. **31**(12), 1821–1823 (2006).
141. N. Sredar, K. M. Ivers, H. M. Queener, G. Zouridakis, and J. Porter, "3D modeling to characterize lamina cribrosa surface and pore geometries using in vivo images from normal and glaucomatous eyes," Biomed. Opt. Express **4**(7), 1153–1165 (2013).

Biomedical Optics EXPRESS

142. Z. M. Dong, G. Wollstein, B. Wang, and J. S. Schuman, "Adaptive optics optical coherence tomography in glaucoma," Prog. Retin. Eye Res. **57**, 76–88 (2017).
143. Z. Nadler, B. Wang, J. S. Schuman, R. D. Ferguson, A. Patel, D. X. Hammer, R. A. Bilonick, H. Ishikawa, L. Kagemann, I. A. Sigal, and G. Wollstein, "In vivo three-dimensional characterization of the healthy human lamina cribrosa with adaptive optics spectral-domain optical coherence tomography," Invest. Ophthalmol. Vis. Sci. **55**(10), 6459–6466 (2014).
144. Z. Nadler, B. Wang, G. Wollstein, J. E. Nevins, H. Ishikawa, R. Bilonick, L. Kagemann, I. A. Sigal, R. D. Ferguson, A. Patel, D. X. Hammer, and J. S. Schuman, "Repeatability of in vivo 3D lamina cribrosa microarchitecture using adaptive optics spectral domain optical coherence tomography," Biomed. Opt. Express **5**(4), 1114–1123 (2014).
145. R. J. Zawadzki, S. S. Choi, A. R. Fuller, J. W. Evans, B. Hamann, and J. S. Werner, "Cellular resolution volumetric in vivo retinal imaging with adaptive optics-optical coherence tomography," Opt. Express **17**(5), 4084–4094 (2009).

1. Introduction

In recent years, optical coherence tomography (OCT) [1] has emerged as a powerful imaging technology in biomedicine. OCT fills the previously unoccupied niche in terms of imaging resolution that places it between microscopy and larger scale imaging technologies such as ultrasound or magnetic resonance imaging. OCT relies on a contrast generated by light scattering and allows for imaging with micrometer scale resolution over a depth of several millimeters (or even centimeters in low scattering media). Due to relatively fast image acquisition speeds, thanks to simultaneous parallel detection of photons scattered from the entire imaging depth, OCT does not only provide cross sectional images of tissue but can yield full 3D information of the sample within seconds [2]. One of the main fields of application of OCT is ophthalmology where this technology revolutionized diagnosis and treatment monitoring of many diseases of the posterior segment of the eye, the retina [3,4]. In less than 15 years since its commercialization, OCT has become an indispensable diagnostic tool and many instruments are nowadays commercially available.

The highest achievable transverse resolution for retinal imaging is usually limited by the optics of the eye because it acts as the objective for any optical retinal-imaging instrument including OCT. The main causes for this limitation are the finite size of the eye pupil (introducing diffraction to the imaging light) and imperfections of the optical properties of the eye [5]. The latter introduces aberrations to the wavefront of the imaging light, both static and dynamic, that degrades image quality (sharpness and signal to noise ratio). This effect will be more pronounced in the case of instruments that employ imaging beam diameter that use the entire pupil of the eye and are close to the maximum dilated eye pupil (~7mm) [6–9]. Thus, small imaging beam diameters (below ~2mm) are typically used to minimize the influence of aberrations, which comes at the cost of a relatively low transverse resolution (~15µm for a typical eye). Associated with this transverse resolution is a large depth of focus (DOF), which determines the axial resolution of ophthalmic instruments such as a fundus camera or a scanning laser ophthalmoscope [10, 11]. A clear advantage of OCT for retinal imaging compared to other optical imaging methods is that axial and transverse resolution is de-coupled. The high axial resolution results from the coherent detection scheme of OCT and depends on the axial coherence length of the OCT light source. As outlined below, the coherence length is inversely proportional to the spectral bandwidth of the light source. This allows for clinical retinal imaging with high axial resolution (typically below 5 µm) independent from transverse resolution. In contrast to other imaging modalities a larger DOF is beneficial in OCT as a larger depth range will be imaged sharply. One of the consequences of OCT being a coherent imaging technique is that OCT images are modulated by a high spatial frequency speckle pattern that is usually reduced by spatial, temporal (in the case of a non-stationary sample) or spectral averaging [12–14].

To enhance the transverse resolution of retinal optical instruments the fully dilated pupil of the eye has to be used for imaging to ensure best possible diffraction limited resolution. However, aberrations of the imaging wavefront introduced by the optics of the eye that is imaged prevent a diffraction limited performance. This requires compensation or correction

Biomedical Optics EXPRESS

of these aberrations. This correction can be achieved with adaptive optics (AO), a technology that was originally intended to improve the image quality in ground based telescopes in astronomy [15]. Meanwhile, in ophthalmic applications, AO has been combined with fundus photography [16], scanning laser ophthalmoscopy [17] and OCT [18].

This review gives a short introduction to the underlying technology of AO with specific focus on AO-OCT instrumentation for retinal imaging. Since the introduction of AO-OCT several reviews have been published to cover the detailed history of instrument development and application of this technology [2, 19–24]. Here we provide an overview of the most successful implementations combining AO with OCT and review some of the latest developments in the field including new AO-OCT applications and new technological advances in wavefront sensor less AO-OCT and computational wavefront correction.

2. AO-technology

Classical adaptive optics systems require three different components: A wavefront sensing component, a wavefront correcting component and a controller (usually a personal computer running an AO control software) that links the first two elements together and allows aberration correction through minimization of the residual wavefront error. In some AO systems, the wavefront sensor (WFS) is not used and instead the correction feedback is provided by the quality of acquired images (total intensity or sharpness). These systems are often called wavefront sensor-less AO or sensor-less AO.

2.1 Wavefront sensing

The amount of light that can be delivered safely to the eye is limited by potential photo thermal, photomechanical or photochemical damage and corresponding laser safety standards need to be fulfilled to ensure safe imaging [25, 26]. To allow wavefront sensing, part of the imaging light or a separate light beacon (guide star) is used. AO is not an imaging modality per se. It is a supporting technology providing enhanced performance to retinal imaging modalities like fundus camera, scanning laser ophthalmoscopy (SLO) or OCT. Thus, the light power that needs to be dedicated to wavefront sensing should be kept to a minimum. Although there are several types of wavefront sensors, all wavefront sensor based AO-OCT instruments published so far rely on a Shack Hartman wavefront sensor (SHWS) [27]. The SHWS consists of an array of lenslets placed at the focal distance in front of an area detector (charge coupled device (CCD) or complementary metal–oxide–semiconductor (CMOS)). A planar wave that is incident on the SHWS is used as the reference to produce spots on the camera each corresponding to one of the illuminated lenslets. Any deviations from this reference wavefront will produce displacements of each spot that can be represented in the Cartesian coordinate system of the camera as Δx in x and Δy in y direction. These displacements are directly proportional to the average slope within the area of a lenslet of the wavefront W (x,y) that is incident on the SHWS pupil (lenslet array) and depend on the focal length f of the lenslet array.

$$\frac{\partial W(x,y)}{\partial x} = \frac{\Delta x}{f} \text{ and} \tag{1a}$$

$$\frac{\partial W(x,y)}{\partial y} = \frac{\Delta y}{f} \tag{1b}$$

The reconstruction of the wavefront can then be performed by direct integration of Eq. (1) or through an approximation of the wavefront using a set of polynomials (usually Zernike polynomials) and least square fitting. AO correction does not necessarily require the reconstruction of the wavefront, as minimizing of the slopes (i.e. spot displacements) is sufficient to minimize the wavefront aberrations. As is very common in ophthalmic AO systems, this procedure also requires excluding the influence of tip and tilt. For diffraction

Biomedical Optics EXPRESS

limited imaging removal of tip/tilt is not necessary as it results in a simple lateral shift of the image. There are several critical issues for the choice of the SHWS. First of all, individual subject aberrations strongly vary and in some cases large aberrations are present [9]. Thus a high dynamic range of the wavefront sensor, which can be accomplished, with a short focal length of the lenslets, will be beneficial. On the other hand, the precision of the wavefront measurement will be improved by a longer focal length of the lenslets which usually leads to a compromise between these influences. Since large aberrations (mainly defocus) may be compensated by trial lenses or other means (e.g. Badal-system), longer focal lengths are usually preferred in order to allow for a more precise wavefront measurement. Another issue is the sensitivity of the SHWS to higher radial order wavefront aberrations. The total number of lenslets (that samples the pupil of the eye) determines the highest aberration (such as highest Zernike mode) that can be measured. Ideally, this number matches the number of actuators of the correcting device in order to minimize the amount of light that is needed for wavefront sensing. However, this requires an exact alignment of the lenslets in respect to the location of the actuators. A more practical approach requires an oversampling of the lenslets by a factor of 2 [28].

Light detected by the SHWS might originate from different sample depths. This may cause problems in wavefront sensing for samples that highly scatter light over an extended depth range (such as imaging the optic disc in humans or in experimental animals, rat or mouse, with relatively thick retinas and varying levels of pigmentation). Thus, some groups proposed the use of a coherence gated wavefront sensor that provides a similar depth resolution for the wavefront measurement as is known for OCT [29, 30].

2.2 Wavefront correction

A variety of different devices are available for shaping the wavefront of an imaging beam. The most common correcting device used in AO-OCT is a deformable mirror (DM) with a continuous mirror membrane [18, 31–35]. However, other correcting devices such as a liquid spatial light modulator [36] or segmented mirrors [37, 38] have been used as well. The high variability of ocular aberrations in the population sets specific demands on the correcting device. Some groups proposed the use of two DMs with different specifications in order to account for this [39, 40]. Thereby, a DM that consists of few actuators but has a large stroke is implemented to correct for larger amplitude low order aberrations (such as defocus and astigmatism). The second mirror consists of many actuators with lower stroke, which enables the correction of higher order aberrations. Together these two deformable mirrors can compensate a large variety of aberrations. Because of the similarity to the extension of the frequency range for loudspeakers this configuration is often referred to as “woofer (first DM)-tweeter (second DM)” system. Nevertheless, a dual DM configuration increases instrument complexity and costs. In general there are several specific requirements for all wavefront correctors applied in retinal imaging and these requirements also apply to AO-OCT systems [41].

2.3 Wavefront sensor based AO-correction

For an efficient AO-correction the wavefront exiting the eye pupil needs to be carefully imaged onto the SHWS, the DM and the detection pupil (collimator lens in the sample arm of the OCT system). In addition, the pupil plane of the eye needs to be imaged (optically conjugated) onto the pivot axes of the x and y scanners. To achieve this condition optical telescopes (based on spherical mirrors [32] or on lenses [42]) are used which are placed usually in 4f configuration between the individual components. Since aberrations introduced by the eye vary with time [43], it is desirable to control the AO system at high AO correction bandwidth during imaging (10 Hz or more) [44]. This bandwidth is limited by the exposure time of the SHWS (which amongst others depends on the amount of light that is dedicated for wavefront sensing) and the computational efforts for AO correction. The response time of the

Biomedical Optics EXPRESS

mirrors typically lies in the kHz range. Apart from few early AO-OCT systems [18, 36] most recent systems use AO correction in a closed loop mode operating at several Hz. In order to determine the correction efficiency of an AO system the root mean square (RMS) error of the residual wavefront can be estimated by the SHWS. In principle, direct far field measurements of the point spread function (PSF) can be performed as well [45]. Figure 1(a) shows a typical RMS wavefront error measurement during AO-correction with a 2 DM AO-OCT system at 840nm [39]. The initial RMS error value of 0.4µm can be reduced to values around 0.06µm after a few iterations. This corresponds to reduction of aberrations to the level of diffraction-limited imaging. According to Maréchal criterion a RMS value below λ/14 (= 60nm for 840nm central wavelength) is considered as diffraction limited [46].

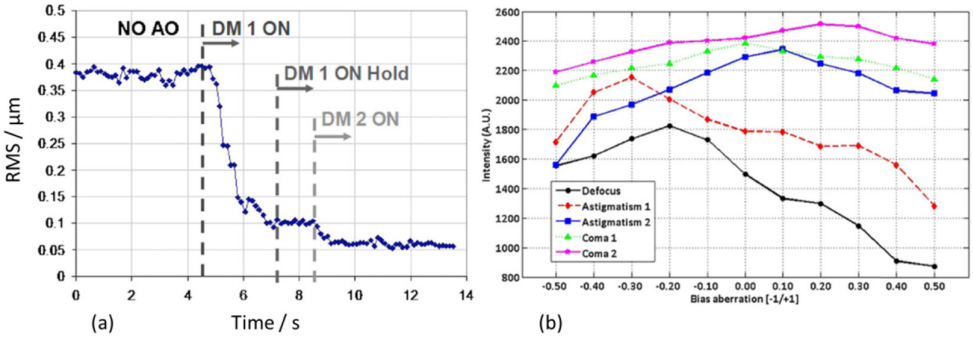

Fig. 1. a.) Evolution of the RMS error of the measured wavefront during AO-correction of a dual DM AO-OCT system operating at 840nm (adapted from [39] with the permission of the Optical Society of America). b) Search result for optimum aberration correction in a wavefront sensor less AO OCT system. Changing the amplitude of the consecutive Zernike modes alters the wavefront at the pupil plane. The DM introduces these while changes in image intensity are monitored. (Reproduced from [47], with permission from Wolters Kluwer Health, Inc).

2.4 Wavefront sensor less AO correction

For most wavefront sensor less AO-OCT systems the OCT image itself (acquired in real time by the AO-OCT system) is used to assess the effect of changing the wavefront (shape of the DM) [48–52]. Therefore, the image quality itself replaces the wavefront sensor as sensing element of these AO systems. Thereby, different image metrics such as intensity or sharpness can be used. Wavefront sensor less AO holds promise of great simplification of AO-OCT systems because there are no restrictions on the use of optical elements for imaging. Lenses usually give rise to unwanted reflections on the wavefront sensor and thus erroneous wavefront measurements that can only be eliminated by implementation of additional optics such as polarization sensitive components [53]. One drawback of retinal wavefront sensor less systems is that aberrations (usually decomposed into individual Zernike modes) are commonly compensated serially, which makes these systems rather slow. Thus, the ability to correct for temporally varying aberrations is greatly reduced. This limitation implies that the temporal performance of wavefront sensor less AO systems needs to be greatly improved in order to fully replace hi-end WFS based AO-OCT. New algorithms are currently developed that significantly shorten the time that is needed for sensor less wavefront correction [54]. In combination with low cost correcting devices (such as an adaptive lens [52]) these systems might be able to provide sufficient improvement of image quality at costs that can be commercially feasible for next generation clinical OCT systems [55]. Another aspect that needs to be considered is the requirement of higher total light exposure of the retina during the AO-correction process by wavefront sensor less AO, due primarily to the longer AO correction time required. In this respect, the use of a separate light beacon for the sensor in SHWS systems can also be beneficial because it allows in principle to turn off the imaging

Biomedical Optics EXPRESS

light until full correction is achieved. Wavefront sensor less AO has recently been implemented in wide-field retinal OCT to enhance imaging of targeted regions [56]. A similar concept has been applied for defocus and astigmatism correction using a Badal optometer and a liquid crystal device, respectively [57]. Figure 1(b) shows a representative result of a search of aberrations in a human subject with a wavefront sensor less AO OCT instrument.

2.5 Computational wavefront correction

As coherent imaging technique, OCT has access to the phase of the light field allowing detection of the full electric field returning from the sample. Hence the phase can be manipulated in post-processing which in principle would eliminate the need of a correcting device in the optical setup. There are an increasing number of papers investigating the possibilities of the so-called "computational" or "digital" correction of aberrations in OCT data [58–62]. The algorithm can be applied either to OCT B-scans or OCT volume data. However, phase stability during data acquisition is a fundamental requirement of these techniques. While this can be easily achieved in microscopy settings, it is very challenging for *in vivo* retinal imaging because this requires very high acquisition speeds (volume acquisition rates in the order of hundreds of Hz). The combination of swept source OCT with full field OCT yields high acquisition rates and efficient data acquisition due to a lack of confocal detection (which otherwise results in rejection of out of focus light during data acquisition). This allowed for efficient correction of ocular aberrations for retinal images acquired *in vivo* using post processing techniques [62]. Recently, an interesting effect could be observed when using full field OCT in combination with a spatially incoherent light source [63]. In such a system, aberrations will affect only the signal intensity and not the image sharpness.

A clear advantage of computational methods is the possibility to correct for defocus for each imaging depth. Thus, the limited depth of focus, inherent to high-resolution systems, may be overcome and 3D volumes with high resolution can be computed that maintain sharpness throughout imaging depth. One clear drawback of these methods is the requirement of very high imaging speeds. Thus the sensitivity is in general quite low which is impractical for most clinical OCT applications. In addition, it might be necessary to pre-compensate for large aberrations (such as defocus or astigmatism) using for example corresponding trial lenses. Nevertheless, first proofs of principle are promising and future developments in the field may result in the construction of clinically applicable next generation AO-OCT systems.

3. AO-OCT technology

3.1 Axial and transverse resolution of AO-OCT

The axial resolution of OCT (Δz) is defined as the full width at half maximum (FWHM) of the double pass coherence length of an OCT system. In the case of a Gaussian shaped spectrum the axial resolution can be calculated via [64]

$$\Delta z = \frac{2ln2}{\pi}\frac{\lambda_c^2}{\Delta\lambda} \tag{2}$$

where λ_c denotes the central wavelength of the light source and $\Delta\lambda$ the corresponding FWHM bandwidth. Implementation of AO-correction requires several additional elements in the sample arm of an OCT interferometer. Apart from matching the optical path length which can be several meters long, dispersion and the corresponding degradation of axial resolution [65] are a critical issue. Thus, dispersion needs to be compensated by introducing corresponding material into the reference arm of the OCT interferometer. For an OCT system operating at 840nm and a FWHM bandwidth of 50nm the theoretical axial resolution is 4.5µm in tissue (assuming a refractive index of 1.4).

Typically, OCT uses light emitted from a single mode fiber, which will have a Gaussian intensity profile. Thus, it is common in OCT to define the transverse resolution via Gaussian

Biomedical Optics EXPRESS

beam optics [64]. However, in AO-systems, the full (dilated) pupil of the eye (corresponding to the objective lens in microscopy) will be illuminated. As such diffraction will occur at the pupil edge, which deteriorates the Gaussian beam. Therefore, the transverse resolution needs to be defined via diffraction theory [66]. In truly confocal systems a confocal pinhole that is much smaller than the size of the Airy disc is used in order to increase the lateral resolution compared to classical microscopy. The transverse resolution $\Delta x_{confocal}$ can then be calculated using the focal length f of the objective lens, the central wavelength of the light source λ_0, the entrance pupil diameter D and the refractive index n [66]:

$$\Delta x_{confocal} = \frac{0.44 \cdot \lambda_0}{NA} \approx \frac{0.88 \cdot f \cdot \lambda_0}{n \cdot D} \tag{3}$$

In this equation we approximated the numerical aperture NA with nD/2f. In order to define the lateral resolution in a similar way as the axial resolution of OCT, the FWHM of the lateral point spread function can be calculated by [66]:

$$FWHM_{confocal} = 0.84 \Delta x_{confocal} = \frac{0.37 \cdot \lambda_0}{NA} \tag{4}$$

which yields the same expression as can be found in the OCT handbook [67]. However, the collimator in the illumination/detection arm of an OCT interferometer has a higher or a same numerical aperture than the single mode fiber in order to increase the collection efficiency of the fiber. Thus, the system cannot be considered truly confocal anymore (the confocality depends on the size of the detector [68]) which degrades transverse resolution down to the level of a classical microscope [69, 70]. Using the same definition via the FWHM of the lateral point spread function the lateral resolution in OCT (without confocality) can then be expressed via

$$\Delta x_{OCT} = \frac{0.51 \cdot \lambda_0}{NA} \approx \frac{1.02 \cdot f \cdot \lambda_0}{n \cdot D} \tag{5}$$

It should be noted that Eq. (5) refers to the FWHM of the lateral point spread function of the intensity. Owing to the interferometric detection scheme of OCT, the axial resolution as defined in Eq. (2) refers to the FWHM of the axial point spread function of the OCT amplitude. Figure 2(a) shows the calculated (using Eq. (5)) diffraction limited transverse resolution in the eye in dependence of the pupil diameter for different wavelength regions (assuming that the pupil is the limiting aperture of the system). Thereby, a focal length of 22.2mm and a refractive index of 1.33 were assumed for the eye. With a pupil diameter of 7mm and 840 nm imaging wavelength a transverse resolution of 2µm is achieved. The transverse resolution for the same pupil size is degraded to 2.55µm for a 1060nm imaging wavelength. Associated with the high transverse resolution is a limited depth of focus. The depth where the transverse resolution is degraded by a factor of $\sqrt{2}$ (which can be neglected) is approximated through Gaussian beam optics via the Rayleigh range z_R:

$$DOFz_{OCT} = 2z_R = \frac{2\pi \cdot \Delta x_{OCT}^2}{\lambda_0} \tag{6}$$

where we considered the transverse resolution Δx_{OCT} as the minimum beam waist. For a 7 mm pupil the DOF_{OCT} are 30µm and 39µm for the 840nm and 1060nm wavelength range, respectively. Associated with the relatively small DOF_{OCT} for larger pupils is the problem that only a small portion of the retina will be in focus and imaged sharply. Correspondingly, several OCT volumes with different focus position have to be recorded in order to visualize different structures that are separated in depth such as photoreceptors or nerve fiber bundles. Some approaches have been introduced to overcome the limitation of a small DOF using

Biomedical Optics EXPRESS

multiple beams [71] or an axicon lens [72]. However, these methods have been applied mainly to skin imaging and a translation of these techniques to retinal imaging is not straight forward.

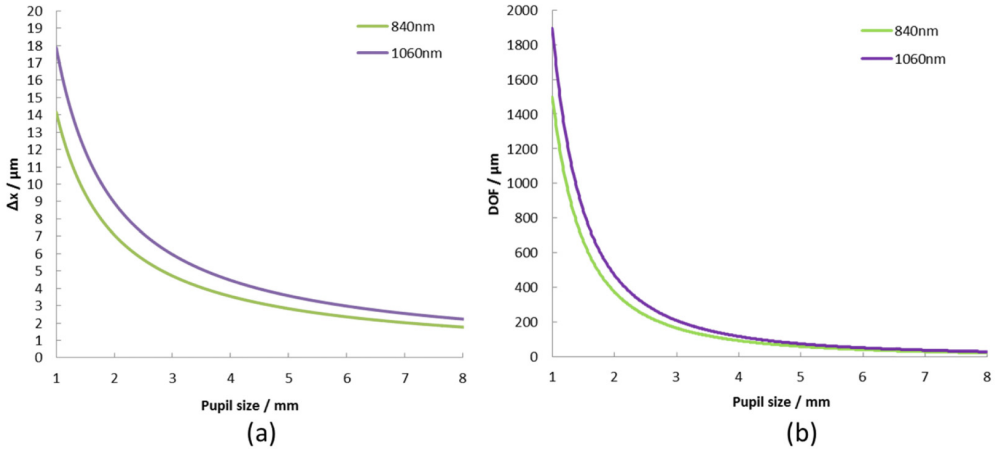

Fig. 2. a) Diffraction limited transverse resolution of AO-OCT in the retina in dependence on the pupil size of the eye for different wavelength regions (assuming that the pupil of the eye is the limiting aperture of the system). b) Depth of focus (DOF) of AO-OCT in dependence on the pupil size of the eye.

Figure 3 shows the effect of different transverse resolutions on the retinal image quality for "standard" clinical OCT images (acquired with a ~1.5 mm imaging beam diameter at the pupil) and AO-OCT images (acquired with a ~7 mm imaging beam diameter and AO correction). The effect of reducing the average speckle diameter as well as the limited depth of focus for images acquired with AO-OCT is clearly visible as a shift in the focal plane is needed to image different depth structures in the retina sharply and with high signal to noise ratio.

3.2 *Chromatic aberration*

AO corrects for monochromatic aberrations. OCT uses light with a broad spectral bandwidth in order to achieve high axial resolution (cf. Equation (2)). Therefore, only the central wavelength is corrected optimally and chromatic aberrations need to be considered as well.

Biomedical Optics EXPRESS

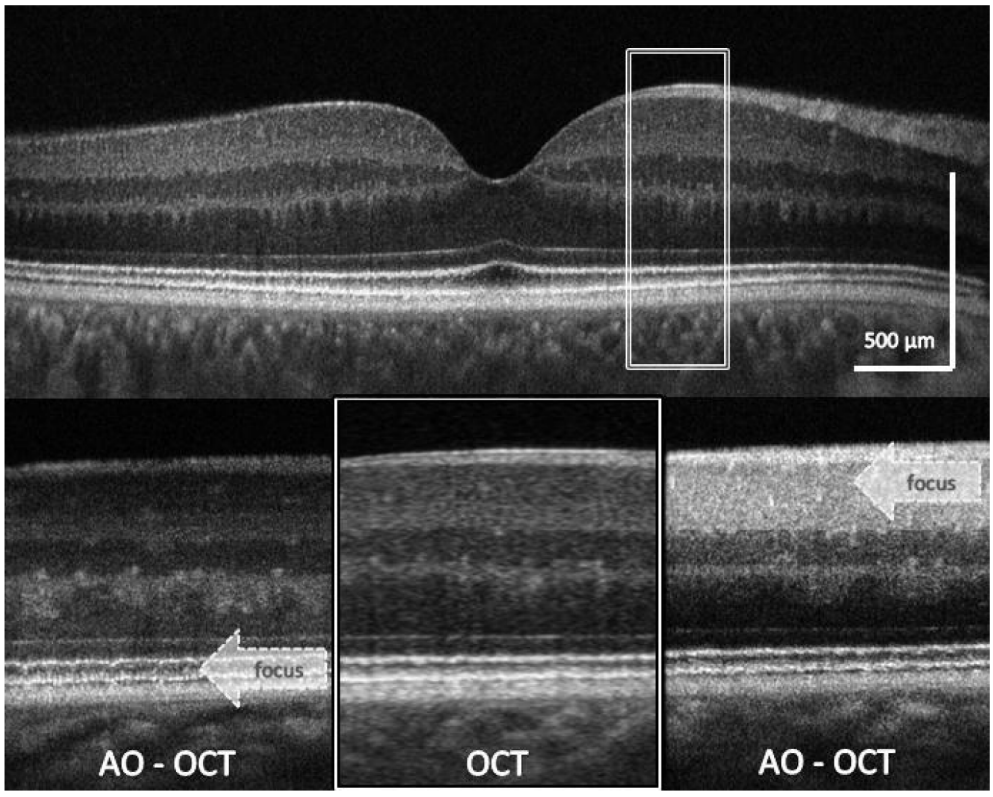

Fig. 3. OCT B-scans of the retina obtained with different imaging techniques. (Top) Clinical OCT acquired over 5 mm; (bottom left) AO high-resolution spectral-domain OCT (0.5 mm scanning range) with focus set at photoreceptor layer; (bottom center) enlarged area (0.5 mm) from the clinical OCT; and (bottom right) AO high-resolution spectral-domain OCT (0.5 mm scanning range) with focus set at ganglion cell layer. The corresponding areas of the bottom images are similar. (Reproduced from [2], with permission from Wolters Kluwer Health, Inc.)

Chromatic aberration affects the axial position of the focus (longitudinal chromatic aberration (LCA)) [73] as well as the different refraction during scanning (transverse chromatic aberration (TCA)) or when imaging the eye at an off chromatic axis position [74]. Both effects cannot be neglected when imaging is done at 840nm with bandwidths that are much larger than ~50nm [75]. In the visible range LCA can be as large as ~2.5 diopters between 400nm and 700nm [73] while in the infrared region this value is reduced to ~0.4 diopters between 700nm and 900nm [75]. In order to compensate for LCA in OCT imaging an achromatizing lens can be employed [35, 76]. This lens introduces a wavelength dependent defocus of the imaging beam that will be compensated by the chromatic aberrations of the eye. Thus high transverse resolution can be achieved even for very large bandwidths. Similar to LCA, TCA depends on the separation between imaging wavelengths and can be quite pronounced when visible light (543-711nm) and infrared light (842nm) is used simultaneously [77]. For TCA compensation the eye needs to be displaced laterally [76]. However, for typical OCT imaging in the 840nm wavelength range (using ~50nm bandwidth) TCA is relatively small and can be neglected for small scanning angles (~1°).

3.3 Field of view and motion correction

The field of view (FOV) of all AO instruments is limited to a few degrees on the retina. The main reason is a limited iso-planatic angle [78]. Within this angle aberrations introduced by the eye vary within a range that will not deteriorate the wavefront below diffraction limit. Its

Biomedical Optics EXPRESS

averaged value can be considered as constant and thus will be properly corrected using AO. For larger scanning angles, the aberrations will vary across the field and cannot be compensated for the entire FOV at once without additional efforts. The iso-planatic angle strongly depends on the subject (and pupil size) as well as the imaging wavelength and varies from 0.5° up to 2° for a pupil size of 6mm [78]. For a smaller pupil size, aberrations will be less pronounced and the iso-planatic field will be larger. The usable FOV may be increased using multi conjugate AO [79]. Another limiting factor for the FOV in AO-OCT is the available A-scan rate. This issue will be most relevant if volumetric imaging is desired. Typical AO-OCT instruments provide transverse resolution of 2µm for a field of view of ~1°x1° which corresponds to an area of ~300x300µm^2 on the retina. In order to provide a sufficient sampling of this area, according to Nyquist theorem, a spacing of ~1µm or smaller between A-scans is required. Thus, a minimum A-scan rate of 90 kHz is required to scan the region within 1 second. A doubling of the scanning angle would require 4x90 kHz = 360 kHz A-scan rate. In addition, distortions introduced by eye motion will be more pronounced with higher magnification (especially in the *en face* imaging plane) which sets further demands on AO-OCT volume acquisition rates. Residual motion can be even observed in images of AO-SLO instruments that operate at much higher *en face* frame rates (~30 frames per second or more) [80]. However, most of these image distortions can be corrected in post processing [80]. To achieve a comparable sampling density and *en face* (volume) recording time an A-scan rate of 30x90 kHz = 2.7 MHz needs to be used. Such high speed has been achieved in OCT only without AO using high speed swept laser sources [81]. Recently an instrument has been introduced that achieves 1MHz A-scan rate for AO-OCT using an optical switch and 4 separate spectrometer [82]. However, at these high speeds the achieved sensitivity was rather low (~70-73dB) which may be problematic for visualization of inner retinal layers.

Several methods have been proposed in order to correct for eye motion in AO-OCT. Some of these are based on image post processing [83], implementation of an additional AO-SLO channel [42, 84] or dynamic retinal tracking [85]. Nevertheless, the efficiency of all these methods increases with image acquisition speed.

3.4 AO in combination with different OCT techniques

There are a variety of different OCT techniques available. Most of them have been combined with AO. The first demonstration of AO-OCT has been performed with time domain techniques, a coherence gated AO fundus camera [86] and a scanning OCT system [18]. The latter was operated at very low speeds (125-250 Hz), which prevented 3D imaging within reasonable time. Imaging speed could significantly be improved with the implementation of Fourier Domain OCT technology because this technique provides higher sensitivity than its time domain counterpart [87–89]. In 2005 three independent groups demonstrated spectral domain OCT in combination with AO using a standard scanning [32, 36] or a parallel line field approach [31]. In order to show the benefit of AO correction, a representative AO-OCT image recorded in a healthy volunteer is displayed in Fig. 4. The focus was set to the photoreceptor layer, which resulted in rather blurred inner retina layers. The zoom in to the photoreceptor layer (cf. Figure 4(b)) shows a discrete spacing of high reflective spots in the IS/OS and the COST bands that correspond to individual cone photoreceptors. For a justification of the labeling of the outer retinal bands we refer to previous work of R. Jonnal et al. [90]. It should be noted that the axial position of individual cone photoreceptors varies. The signal originating from the RPE corresponds to a diffuse speckle pattern. Since the A-scan rate of these systems was limited, mainly B-scans or very small volumes have been recorded.

Biomedical Optics EXPRESS

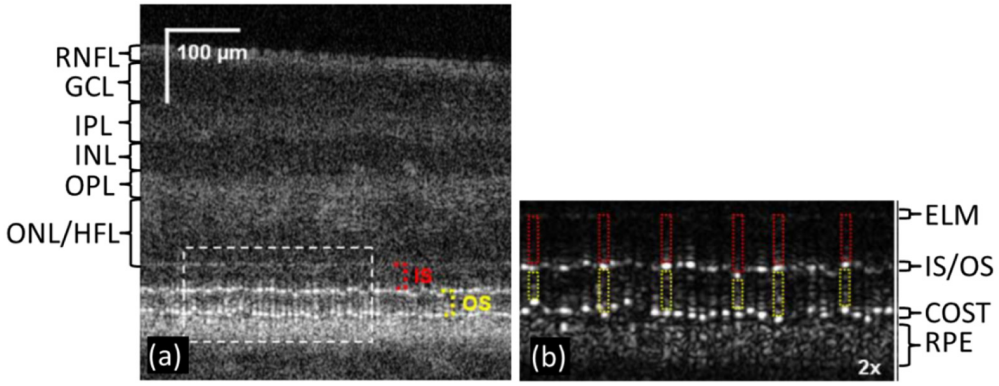

Fig. 4. A) Representative AO-OCT B-scan with the focus set to the photoreceptors recorded in a healthy volunteer at 4.5 nasal eccentricity from the fovea (logarithmic intensity grey scale). B) 2x enlargement of the region marked with the white rectangle displayed on a linear intensity scale (some inner and outer segments of cones are marked with red and yellow rectangles, respectively). The retinal layers are labeled as follows: RNFL retinal nerve fiber layer, GCL ganglion cell layer, IPL inner plexiform layer, INL inner nuclear layer, OPL outer plexiform layer, ONL/HFL outer nuclear layer/Henle's fiber layer, ELM external limiting membrane, IS/OS junction between inner and outer segments of cone photoreceptors, COST cone outer segment tips, RPE retinal pigment epithelium (adapted from [76] with the permission of the Optical Society of America).

For high resolution applications that are associated with a low DOF other OCT approaches such as *en face* OCT [91] may proof advantageous. The *en face* recording time of these systems is typically very fast (several frames per second) and analogous to SLO imaging. Thus, both imaging modalities can be used simultaneously, which simplifies motion correction [33, 92]. Slow scanning in *en face* OCT is performed along the depth direction which enables the implementation of a dynamic focus [93] and thus the maintenance of high transverse resolution throughout imaging depth. However, the main drawback of this technique is the requirement of a high-speed axial eye tracker [94, 95]. The combination of *en face* OCT/SLO with AO allows the visualization of rods and foveal cones [42]. Figure 5 shows representative images of the fovea region recorded with an *en face* OCT system. Owing to the high dynamic range of the cones in this area of the retina, the images are displayed on a logarithmic intensity scale as has been proposed by A. Dubra et al. for AO-SLO images [96]. The pixel-to-pixel correspondence between AO-SLO and AO-OCT allows for a direct comparison of both imaging modalities. The cone mosaic in the fovea area where the packing density is highest can be clearly seen in the images recorded with both techniques.

With the development of faster OCT systems, 3D imaging based on scanning Fourier domain OCT became feasible [39, 97]. Currently most AO-OCT systems are based on the Basler camera, which allows for A-scan rates between 100 and 250 kHz [98–101]. Using four independent spectrometers (and 4 separate cameras) in combination with an optical switch, the duty cycle of the system can be optimized to 100% and A-scan rates of 1MHz have been realized [82].

Most of the AO-systems reported so far used light in the spectral range around 750-950 nm. Application of shorter wavelengths is associated with higher transverse resolution (cf. Equation (5) and is thus preferable from a pure imaging resolution standpoint. However, shorter spectral regions lie already in the visible range and the subjective perception of the light power will increase manifold (the absorption spectra of the photo-pigments in the retina have their corresponding peaks in the visible range) leading to discomfort of the imaged subject. In addition the laser safety standards describing light tissue interaction for visible wavelength regions require that in addition to a photo-thermal limit a photochemical limit

Biomedical Optics EXPRESS

needs to be considered. Thus, the total light power that can be applied safely to the eye is greatly reduced in this wavelength region, which results in a reduced sensitivity of the system.

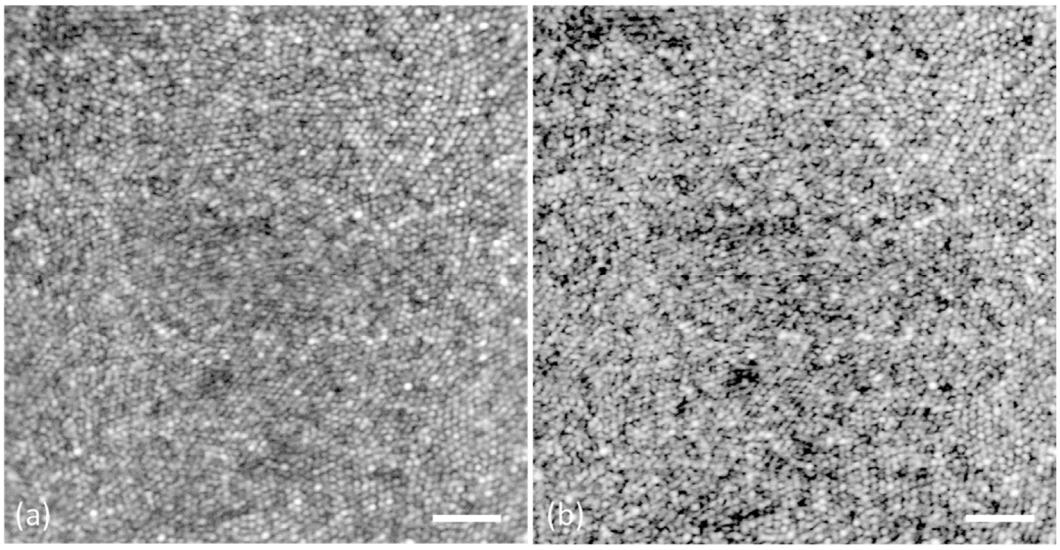

Fig. 5. Representative en face images of the fovea of a healthy volunteer recorded with an AO-SLO/OCT instrument. (a) AO-SLO-image, (b) depth integrated AO-OCT image including following outer retinal layers: ELM, IS/OS, COST, and RPE. The images are displayed on a logarithmic scale in order to account for the high dynamic range of the image. Scale bar: 30µm (adapted from [42], with the permission of the Optical Society of America).

The use of light at longer wavelength regions is associated with less scattering in tissue but with higher absorption by water (the main constituent of tissue). The wavelength region around 1060nm lies within a local minimum of the water absorption bands and is widely used to enhance the penetration depth of retinal OCT imaging [102, 103]. However, light detection at this wavelength region requires line scan cameras that are based on a different material (InGaAs instead of silicon). The commercial use of these cameras is less widespread and thus these cameras are much more expensive than their silicon based counterpart. A first proof of concept of AO-OCT at this wavelength region together with a comparison of AO-OCT at 840nm has been presented in 2010 [104, 105]. The concept was then extended for imaging of choroidal vessels [106]. At the 1060nm wavelength region the use of swept source OCT certainly is more attractive as the sensitivity roll off with depth is less pronounced (or even eliminated) with this technology. This roll off arises from the finite pixel size of the line scan detector in the spectrometer and the dispersion of the recorded spectrum in the wavelength (λ) domain. In order to eliminate this roll off, the spectrum needs to be recorded in the $1/\lambda$ domain as can be achieved with SS-OCT [107]. SS-OCT at 1060nm has been combined with AO in a multimodal instrument [105] and a wavefront sensor less approach [108]. Finally, many different combinations of the above mentioned AO-OCT systems with complimentary imaging modalities have been presented [33, 34, 40, 84, 92, 105].

4. AO-OCT in healthy volunteers

4.1 Imaging of outer retinal layers

The high axial resolution provided by OCT allows for a clear separation between the different outer retinal layers. This is a clear advantage compared to AO-SLO or AO-fundus camera imaging. Figure 6 shows representative images of different retinal layers in the foveal region. The cone mosaic is clearly visible at IS/OS and at COST indicating wave-guiding properties of cone photoreceptors. Light is coupled into a cone inner segment ("wave-guide") and

Biomedical Optics EXPRESS

changes in the refractive index within the cone (at IS/OS junction and at the tip of the OS) give rise to these distinct reflections. Wave guiding of cones has been proposed earlier because of the observed directionality of light reflected from cones (or light that may enter cones) which is also known as optical Stiles Crawford effect of the first kind [109] and has been investigated using OCT [110]. This effect has severe implications for determining the cone density in patients as due to changes in elevations of the photoreceptor layer (drusen) and the Stiles Crawford effect the reflectivity of cones can be very weak and as such be misinterpreted as missing cones. Within the RPE a faint regular structure with a lower spatial frequency can be seen indicating the presence of the RPE cell mosaic [42, 101]. In order to improve the visibility of RPE cells, averaging over several AO-OCT volumes recorded at different time points (separated by several minutes) is required. A recent study showed the RPE mosaic visualized with an AO-OCT system in six healthy subjects and at two different eccentricities [111]. The status of the RPE is indicated as a key factor in the development of many outer retinal diseases such as age related macular degeneration (AMD), one of the leading causes for blindness in the industrialized world. Although AO-SLO using dark field detection schemes or autofluorescence imaging yields similar images of the RPE mosaic, AO-OCT is capable of providing simultaneously additional information on the depth extension of these structures and overlying cone photoreceptors [111].

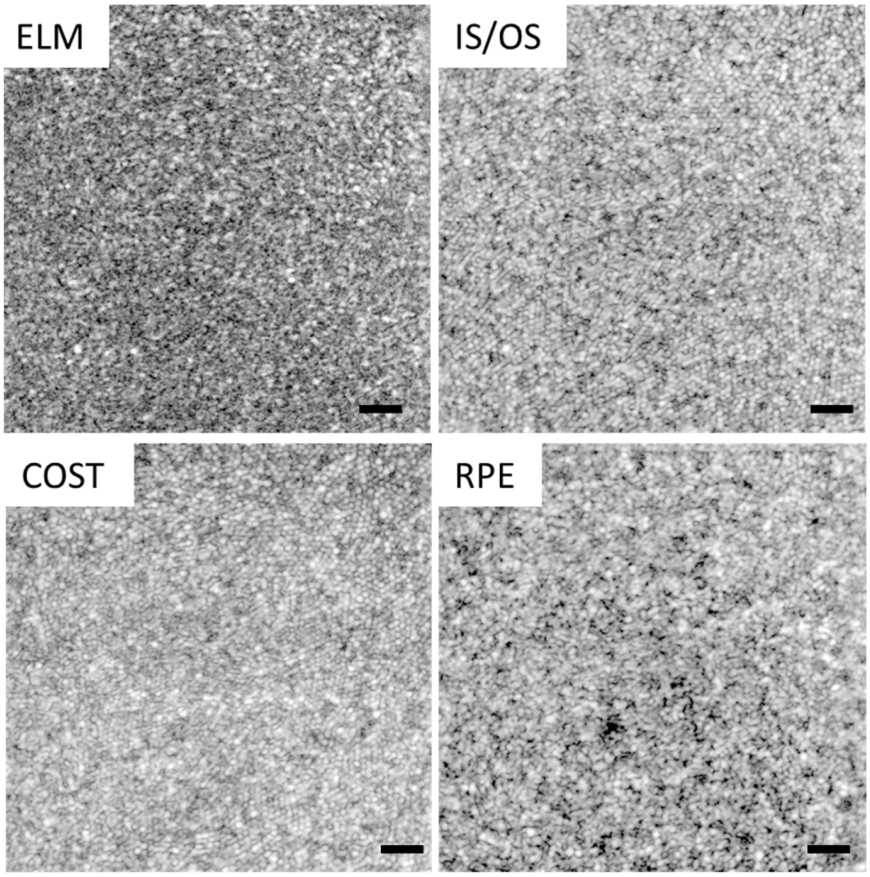

Fig. 6. Representative AO-OCT images of different posterior retinal layers recorded in the fovea region of a healthy volunteer. ELM external limiting membrane, IS/OS junction between inner and outer segments of cone photoreceptors, COST cone outer segment tips, RPE retinal pigment epithelium. All images are displayed on a logarithmic intensity scale. (Scale bar: 30µm, image adapted from [42], with permission of the Optical Society of America).

Biomedical Optics EXPRESS

At larger eccentricities from the fovea rod photoreceptors are present and the size as well as the spacing between cones is increasing. The increasing cone size results in changes in the corresponding wave guiding properties as several wave-guiding modes can be exited [42, 112]. This effect can be seen in some of the cones displayed in Fig. 7(a). The image was recorded with an *en face* AO-OCT instrument at ~8° eccentricity from the fovea at the IS/OS layer. As is known from histology [113] and from ultrahigh resolution OCT imaging [114], the outer segments of cones are slightly shorter than the outer segments of rods. Thus the contribution from both layers can be separated using the depth sectioning capabilities of AO-OCT. Figure 7 shows a composite false color image of the COST (red) and rod outer segment tips (ROST, green) layers.

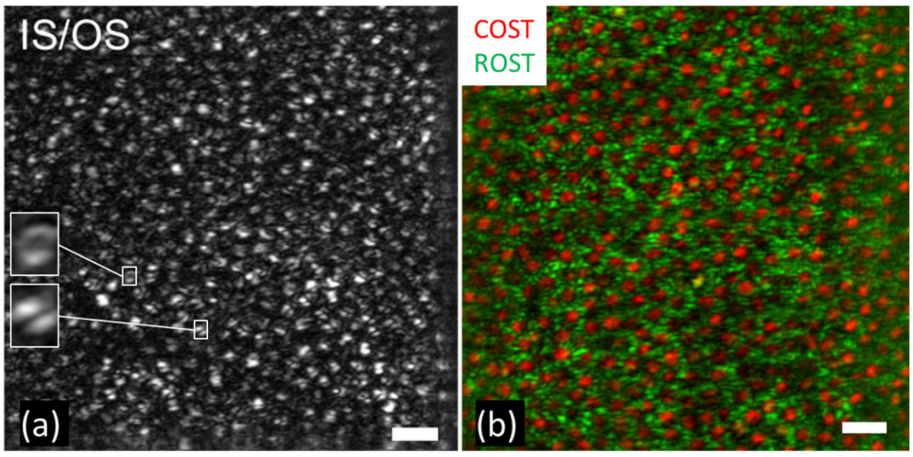

Fig. 7. AO-OCT images recorded at ~8° eccentricity from the fovea. a) Segmented junction between inner and outer segments of cone photoreceptors showing distorted intensity patterns. Some patterns are enlarged (inset) and show intensity distributions that are typical to multimodal wave propagation. b) Composite image of different retinal layers recorded at the same retinal location and displayed in a false color scale. COST layer is indicated in red, rod outer segment tips (ROST) layer is indicated in green. (Scale bar: 30µm, images adapted from [42], with permission of the Optical Society of America).

Changes in the reflectivity of cones at IS/OS or COST provide information on physiological processes of cones. The changes in reflectivity of both layers is not correlated [115] and are believed to depend on the cone renewal process that includes disc shedding and phagocytosis of these discs by the RPE. These processes have been studied in detail in the animal model only because of the invasiveness of the procedure. However, using AO technology this process can now be investigated in vivo [116, 117]. A recent study used AO-OCT to investigate specifically the disc shedding process in more detail [118]. 3D volumes of the cone photoreceptors were recorded during a period of 90 minutes and individual cones were tracked over time. Thereby, some cones exhibit the absence of the COST reflection for a period of ~18 minutes. After reappearance of the COST reflection the outer segment length was reduced by ~2-3µm clearly indicating the disc shedding process of the photoreceptors by the RPE. Very recently, Hillman et al. reported direct in vivo measurements of changes of the axial length of the cones OS due to visible light stimulation [119]. The possible explanation for this process as osmotic swelling of OS due to G-protein activation has been recently proposed [120]. All of these reports suggest that AO-OCT might provide a new and very exciting opportunity to study the function of photoreceptors *in vivo*.

4.2 Imaging of inner retinal layers

The high sensitivity and axial resolution provided by AO-OCT allows for visualization of different inner retinal layers. Of specific interest are the retinal nerve fiber layer (RNFL) and

Biomedical Optics EXPRESS

retinal vasculature. The RNFL plays an important role in Glaucoma diagnosis. The higher transverse resolution of AO-OCT allows for visualization of individual nerve fiber bundles and measurement of corresponding cross sectional profiles [121]. Figure 8 shows representative AO-OCT data where the focus was set to the anterior retinal layers. In Fig. 8(a) individual nerve fiber bundles are clearly visible. In addition small capillaries (indicated with black arrows) can be seen in the enlarged region of interest in Fig. 8(b). Figure 8(c) shows an AO-OCT B-scan recorded with a wavefront sensor less AO instrument [47]. The colored lines show the depth range over which the intensity is averaged in order to produce *en face* maps. The topmost layer (area between the red lines) clearly shows individual nerve fiber bundles (cf. Figure 8(d)). Some of these are indicated with white arrows in Fig. 8(d).

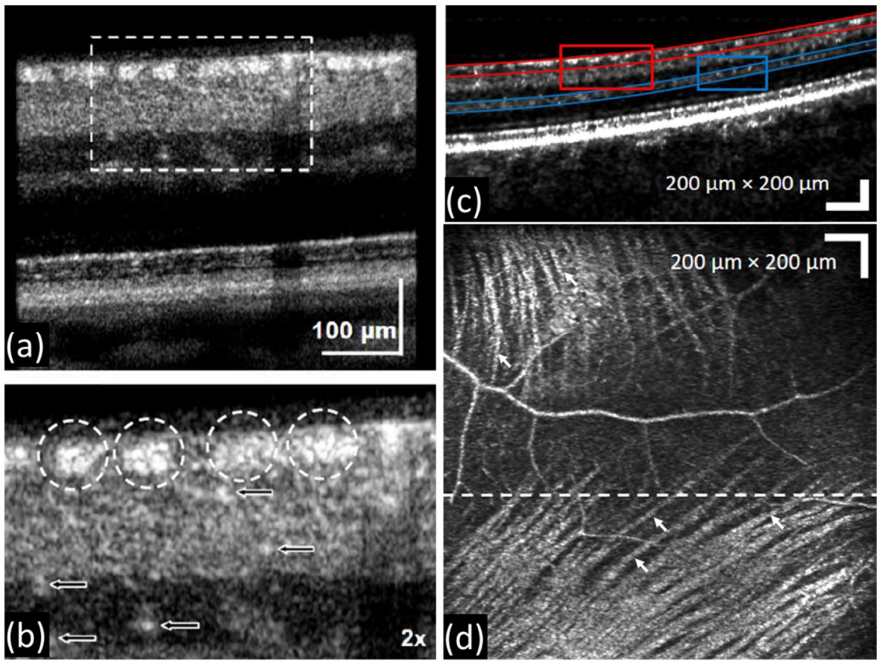

Fig. 8. Representative AO-OCT images of a healthy volunteer with the focus set to the anterior layers. a) Averaged (10 frames) B-scan showing individual nerve fiber bundles. b) Enlarged region (by a factor of 2) of interest indicated with the white rectangle in a). The individual bundles are marked with the white circles. The black arrows indicate micro capillaries in the inner retina. c) Intensity B-scan recorded with a sensor less AO instrument showing different segmentation layers (indicated with different colors). d) *En face* projection of the layer indicated with red lines in c). White arrows point to individual nerve fiber bundles. The dashed horizontal line indicates the location of the B-scan shown in c). a) and b) are reproduced from [76], c) and d) are adapted from [47].

A higher numerical aperture of AO-OCT instruments provides increased contrast of highly scattering blood vessels to the surrounding (weakly backscattering) tissue [32, 95, 122, 123]. However, the contrast can be further increased using angiographic methods as is implemented in standard OCTA imaging [124]. Thereby, several B-scans are recorded at exactly the same retinal location and changes between these images (caused by motion within the capillaries) are visualized. A first proof of concept of AO-OCT angiography (AO-OCTA) has been presented in 2012 [106]. Figure 9 shows a direct comparison between an AO-OCT intensity B-scan and an AO-OCTA B-scan. In the AO-OCTA image static tissue is greatly suppressed and the visibility of small capillaries (some are indicated with a white arrow) is greatly enhanced. Due to the high numerical aperture of the AO-OCT system, shadowing artifacts [125] within the angiographic image as commonly observed in standard OCT

Biomedical Optics EXPRESS

imaging are mitigated. The high resolution of AO-OCTA requires higher B-scan rates compared to OCTA in order to compensate for eye motion that otherwise will cause image distortions. However, the sensitivity to slow flow speeds (as is the case in capillaries) remains the same because the smaller focus of the imaging beam allows to detect changes on a smaller scale than in standard OCT [126].

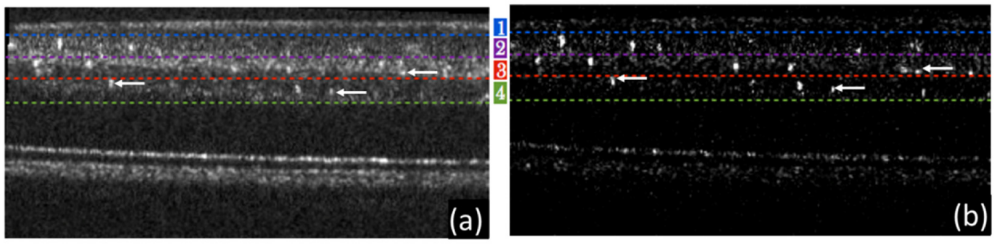

Fig. 9. OCT B-scans recorded with a compact AO-OCT instrument. a) Intensity image (4 frames averaged) showing different segmentation layers (indicated with color bars and labeled with 1-4. b) OCTA B-scan with increased contrast of capillaries. White arrows point to representative capillaries in c) and d) (Images adapted from [126], with permission of the Optical Society of America).

Figure 10 shows *en face* projections (generated by depth integration over the regions indicated in Fig. 9) and provides a direct comparison of vessel contrast between AO-OCT intensity images and AO-OCTA images. Although the vessels show good contrast in the images, the application of OCTA processing further increases the contrast [126]. Especially for tissue regions with high signal intensity from surrounding tissue (such as the nerve fiber layer) the increased contrast is essential for visualizing the vasculature.

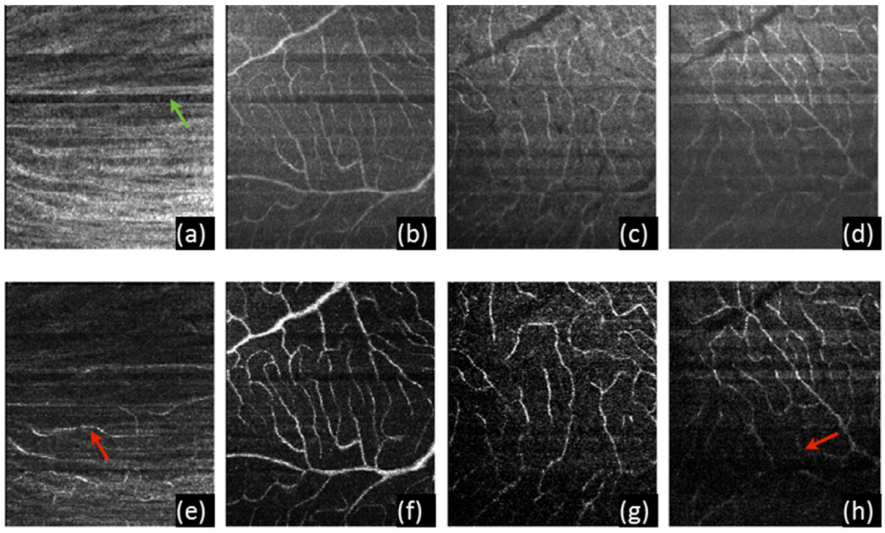

Fig. 10. Comparison between AO-OCT intensity images and AO-OCTA images extracted at different depths. a-d) intensity images generated through depth integration of the depths indicated with numbers 1-4 in Fig. 8. The green arrow indicates an artifact caused by accommodation (and according shift of focus position) of the subject. e-h) Corresponding AO-OCTA images extracted at the same locations as in a-d. (The red arrow in e) points to a vessel that clearly shows increased contrast in this image compared to the intensity image. The red arrow in h) indicates areas with low signal intensity (reprinted from [126], with permission of the Optical Society of America).

Figure 11 shows a comparison of a larger field of view between images recorded with an AO-OCTA and a clinical grade OCTA system in the same healthy volunteer. The larger field

Biomedical Optics EXPRESS

of view of the AO-OCTA was generated through stitching of 25 images that were recorded separately. The higher resolution provided by AO allows resolving of finer details of the vasculature. Since the transverse resolution of standard OCT is around 15µm the true diameter of small capillaries cannot be determined. In addition, projection artifacts are mitigated which enables simplified segmentation of a single vasculature layer.

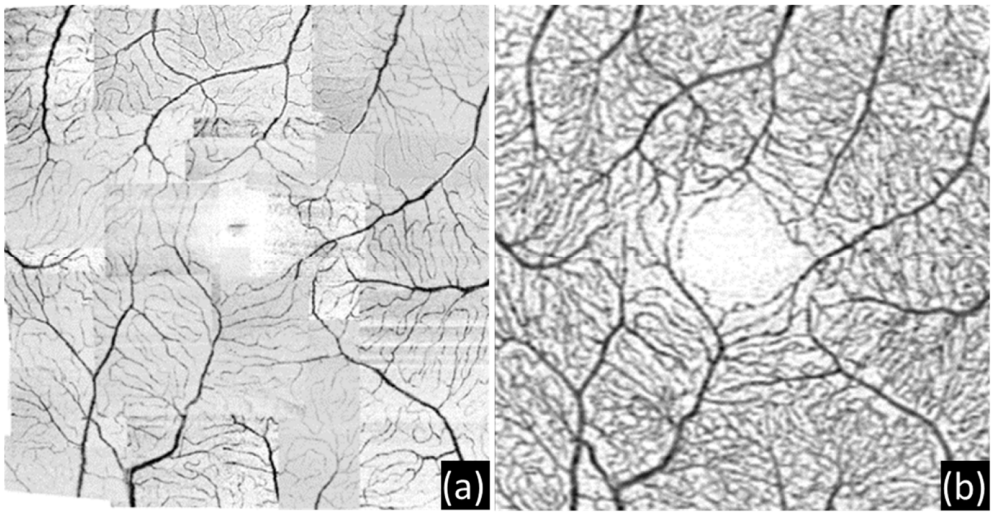

Fig. 11. Comparison of vasculature recorded with different instruments. The images were generated through depth integration of region 2 in Fig. 8 and are displayed on an inverted grey scale. (a) Mosaic AO-OCTA image containing 25 images. (b) OCTA image recorded with a commercial instrument. Field of view: ~7° × 7°. (adapted from [126], with permission of the Optical Society of America).

It would be very interesting to visualize different cell types (such as ganglion cells) of the inner retina. AO-OCT does provide sufficient resolution. However, the contrast of these cells to surrounding tissue is too poor for a clear visualization of such cells. Thus additional techniques are needed in order to provide sufficient contrast. One of these techniques could be polarization sensitive OCT [127]. A first demonstration of PS-OCT in combination with AO has been presented a couple of years ago [128].

5. Clinical applications of AO-OCT

Due to the limited availability of AO-OCT instruments in clinical settings, the clinical potential of AO-OCT is yet still not fully explored. Because of the high magnification of AO-OCT motion artifacts will be much more pronounced which makes imaging of patients with poor fixation capabilities challenging and requires very high imaging speeds. Many diseases severely influence the image quality in AO-OCT such as media opacities, age related miosis or retinal distortions. This greatly reduces the variety of patients that can be imaged. Nevertheless, there is a growing amount of reports on clinical studies using research grade AO-OCT systems due to its potential in diagnoses and treatment monitoring. Several examples are presented below to illustrate the potential clinical value of this imaging technology.

In order to be clinically successful, an imaging technique needs to provide additional insights into frequently occurring eye diseases. One of these eye diseases is AMD that affects people aged 50 years or more. AMD mostly harms the outer retinal structures (photoreceptors, RPE, Bruch's membrane) in the macula. Because of relatively poor fixation capabilities of these patients and frequently present media opacities, imaging of this group of patients with AO-OCT is challenging. Figure 12 shows imaging examples of a patient in a

Biomedical Optics EXPRESS

late stage of AMD, where the macula area already presents with a geographic atrophy (GA) [129]. Several standard clinical tests (see figure caption) were collected on the same eye and are shown in the figure to allow a better assessment of the structural and functional changes of the retina.

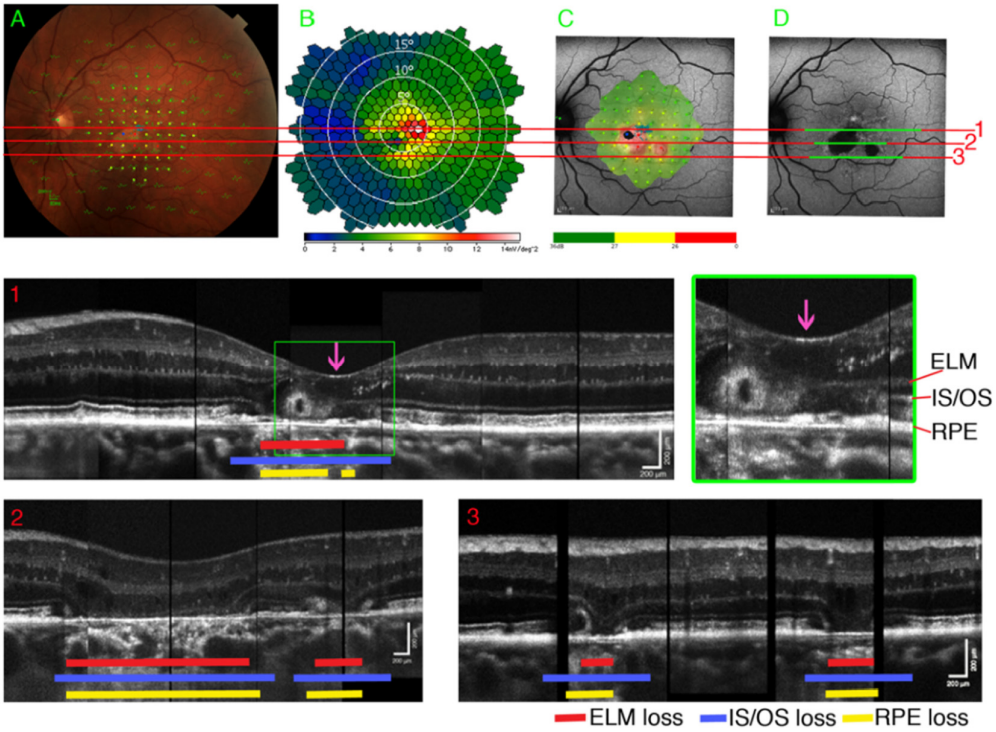

Fig. 12. Application of AO-OCT for evaluating a patient with geographic atrophy. Panel A is the color fundus photograph (CF) with the multifocal electroretinogram (mfERG) traces and micro perimetry (mP) sensitivity superimposed. Panel B shows the mfERG response density map; panel C shows the mP sensitivity map superimposed on the Fundus Auto Fluorescense (FAF), and panel D is the FAF image. The three numbered green lines in panel D correspond to the three B-scan montages shown below. The magenta arrow in B-scan 1 shows the preferred retinal locus of the patient. The red, blue and yellow bars on the B-scans correspond to ELM, IS/OS and RPE loss, respectively. The magnified B-scan section shows remaining RPE that corresponds to the location of the preferred retinal locus [129]. (Reproduced with permission from the Association for Research in Vision and Ophthalmology, Inc (ARVO))

Earlier forms of AMD involve the development of Drusen. The formation and appearance of Drusen and subretinal Drusenoid deposits (SDD) have been investigated with AO-OCT in various stages of AMD [100].

Diabetic retinopathy (DR) is regarded as another frequently occurring eye disease that affects in the US roughly one third of patients with diabetes [130]. In these patients, the visualization of the retinal vasculature is of high clinical interest. AO-OCT angiography is capable to provide detailed images of this vasculature [126].

In other reports AO-OCT was used to study various optic neuropathies, a group of eye diseases that damage the optic nerve, including Glaucoma [131]. Glaucoma is the most common form of optic neuropathy that presents with characteristic loss of visual field due to ganglion cell death. This leads to a thinning of the retinal nerve fiber layer and an excavation of the optic disc. Both parameters are routinely measured using standard OCT. The implementation of AO-OCT bears the potential to visualize the area and volume of individual nerve fiber bundles [121] or to reveal changes in the photoreceptor layer that are accompanied

Biomedical Optics EXPRESS

with the neuropathy [132]. A recent review article discusses the value of AO-OCT for clinical diagnosis of Glaucoma in more detail [133].

Apart from these studies there have been reports of using AO-OCT to investigate inherited degenerative eye diseases. One example is retinitis pigmentosa (RP), a disease that causes abnormalities of photoreceptors (rods and cones) that finally result in a corresponding loss of these cells. AO-OCT studies revealed atrophic regions in the photoreceptor layer with 'drusen like' appearances [134].

Another disease that has been evaluated by AO-OCT is retinopathy of prematurity (ROP), a potentially blinding disorder that alters the development of the central retina and primarily affects prematurely-born infants [135]. This study revealed significant differences to the healthy eye at the fine structural level of the foveal microvasculature. Similarly, changes of the inner retina that are caused by pathologically dilated blood vessels (telangiectasia) near the fovea in idiopathic juxtafoveal macular telangiectasia (MacTel) have been reported [136]. In MacTel, disease progression involves scarring of the retina and accumulation of liquid-filled cysts that in turn compromise photoreceptors and can lead to permanent vision loss.

Apart from a more detailed insight into these retinal diseases, AO-OCT might be of value in cases of vision loss whose cause cannot be determined by standard clinical examination. Initial results in some cases showed, that the greater details provided by AO-OCT, allows for a localization of the source of visual dysfunctions when other methods failed [76]. Additionally, there has been one case report evaluating a patient presenting with multiple evanescent white dot syndrome [137].

Another interesting application of AO-OCT could be to diagnose and study different conditions of color blindness. Normal human color vision relies on three spectrally distinct cone classes. Color vision deficiency, mainly an inherited defect, is usually caused by the absence of one of the classes. The deficiency can also be accompanied with retinal disease and dysfunction of photoreceptors. First imaging results with AO-OCT have been reported in patients with red/green color deficiency due to a Cys203Arg genetic mutation [101].

Finally, we want to emphasize another potential clinical application of AO-OCT: The possibility to monitor structural changes on a cellular level that are associated with stem cell therapy. First image results that show the long term temporal evolution of retinal structures during treatment are promising [134].

6. Commercialization of AO-OCT technology

The impact of OCT in the field of Ophthalmology can certainly be compared with the invention of the direct ophthalmoscopy more than 150 years ago. This is partly due to the very rapid commercialization of this technology. Although OCT instruments are still more expensive than other ophthalmic instruments the success of this technology is based on the applicability to a wide range of patient population and on the cross sectional imaging capability that no other technology can provide. Meanwhile a variety of companies sell OCT instruments and the market is still increasing. On the other hand, the commercial interest in AO-OCT seems to be quite limited. Currently there is only one company that sells research grade AO-OCT instruments [105]. There might be several reasons for that. One is the significantly higher cost of such instruments because additional equipment such as deformable mirrors or wavefront sensors is needed. Both components are still very expensive which puts a commercial AO-OCT instrument at the high price end of ophthalmic instruments. In addition, most of the research grade instruments require a lot of space and highly trained personnel to operate and maintain the instruments in order to achieve the optimum imaging performance. Since space is always very limited in a clinical environment this certainly is an issue. Some groups have addressed this problem by providing compact AO-OCT systems that are of similar size than commercial OCT instruments [40, 138]. Difficulties in commercialization seem to exist for all AO assisted instruments. Currently only an AO assisted fundus camera is commercially available. Although a variety of AO-SLO

Biomedical Optics EXPRESS

instruments are tested in a clinical environment, many of them are research grade systems and only a few of them might evolve into a commercial prototype. Another aspect is the currently limited applicability of the technology to a wide range of patients which is outlined in the next section.

7. Discussion and conclusion

Since the first demonstrations of AO-OCT more than 10 years ago, the technology has been significantly improved in several aspects. Profiting from independent and rapid development of OCT technology, the imaging speed has been increased by an order of magnitude. The stability and resolution of AO-OCT systems has been improved resulting in the visualization of single cells such as cones, rods or RPE cells. Based on the high data acquisition speeds of OCT and increased computational power of state of the art PC's computational aberration correction methods have been developed. It must be noted, however that in young healthy subjects cellular resolution (visualization of the cone mosaic at larger eccentricities from the fovea) can be achieved without the use of adaptive optics as has been demonstrated with fundus photography and OCT [139,140]. Thus the advantages of computational aberration correction methods over hardware based methods (using a DM) remains, at the current stage, unclear. Up to now the cone mosaic has been visualized with these techniques only at larger eccentricities from the fovea and in healthy volunteers. In order to properly compare these two approaches imaging at diffraction limited resolution at full-dilated pupil size (including the visualization of rods and foveal cones) needs to be demonstrated with computational AO.

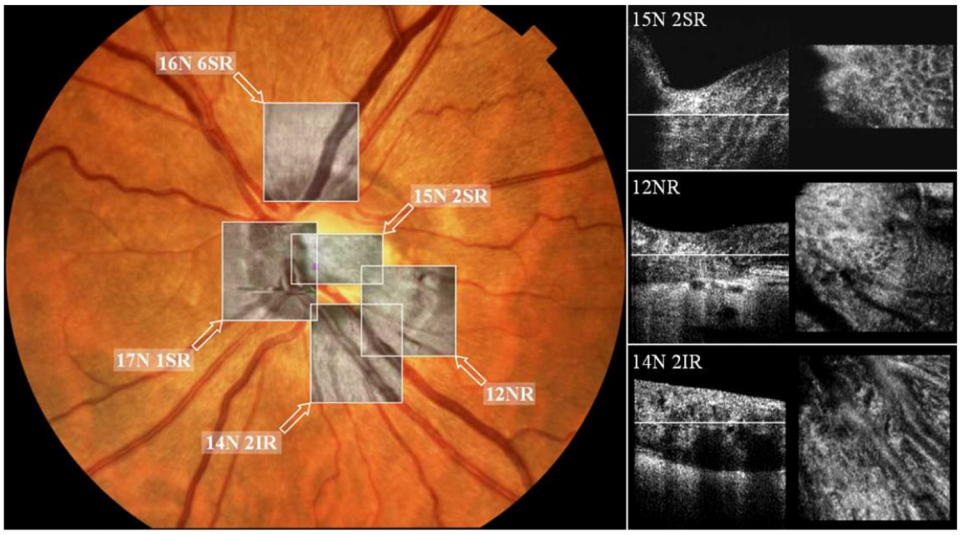

Fig. 13. AO-OCT images recorded in close proximity to the optic disc. The left image shows a fundus photo overlaid with the fundus projections of the different regions of interest that have been imaged with AO-OCT. The right hand side shows representative B-scans and C-scans (the location of the C-scan is indicated with the horizontal white line in the B-scans) retrieved from the OCT volume (reproduced from [145], with permission of the Optical Society of America).

AO-OCT imaging has been mainly performed in the macula area. Imaging close to the optic disc with AO is more difficult because the retinal structures are heavily distorted in this area. This influences the wavefront sensing capabilities of the system. In the macula, light that is backscattered from the photoreceptor/RPE band contributes most to the signal of the SHWS, which results in a reliable wavefront measurement. At the optic disc, the lamina cribrosa, nerve fiber layer and photoreceptor bands will contribute almost equally to the wavefront signal, which will influence the wavefront measurement. Figure 13 shows

Biomedical Optics EXPRESS

representative images recorded in a healthy volunteer of the region close to the optic disc. The high resolution enables the visualization of the pores of the lamina. Changes in the geometry of pores may be an indicator for glaucoma [141]. The pores are a three dimensional structure and changes with depth can be observed using AO-OCT [142–144].

Apart from human retinal imaging experimental animal imaging with AO-OCT has gained interest in recent years [37, 40]. Many retinal diseases can be investigated in corresponding animal models. Non-invasive imaging methods such as AO-OCT will thereby play a key role in animal studies as the same animal can be observed over time, which yields more accurate results and greatly reduces the amount of animals that need to be sacrificed for these studies.

Up to now retinal AO-OCT has been mostly used to image mice. There are several challenges of designing an AO system for an eye that is ten-fold smaller than a human eye. In addition, the availability of highly developed *ex vivo* histochemical retinal imaging methods reduced the clinical demand for non-invasive methods in the animal model. Thus, the development of such instruments started with some delay. AO-imaging of the mouse eye can be seen as part of an ongoing revolution in biological imaging, which is aimed at visualizing cellular structure *in vivo* which allows for studying of retinal function. Remarkably, the mouse eye has an AO-corrected numerical aperture of ~0.5, exceeding that of the human eye by ~2.5-fold, affording exquisite submicron resolution. Figure 14 shows representative image data of the retinal nerve fiber layer of a mouse eye using a sensor less AO system. The wavefront correction increases the signal to noise ratio of the image and improves the visibility of small structures in the image (indicated with white arrows in Fig. 14(b) and 14(c)).

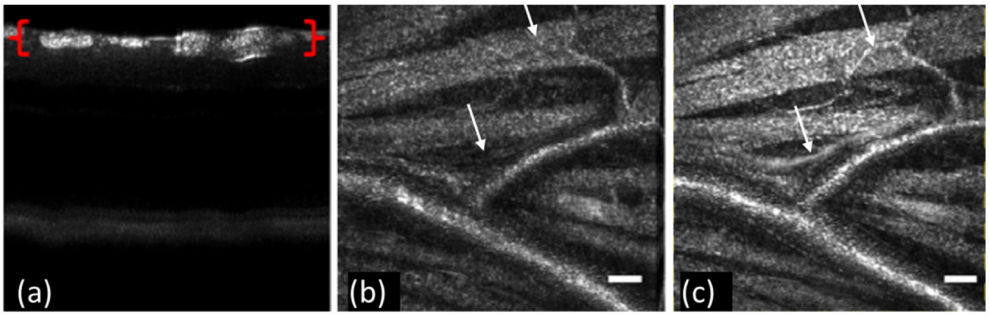

Fig. 14. Representative AO-OCT of the nerve fiber layer of the mouse retina recorded with a wavefront sensor less AO-OCT instrument. a) B-scan showing individual nerve fiber bundles. The red brackets indicate the depth extension that was used for averaging in order to generate the corresponding *en face* images. b) *En face* image of the nerve fiber layer before adaptive optics correction. c) *En face* image of the nerve fiber layer after adaptive optics correction. The white arrows point to structures that are hardly visible in b) but can be clearly seen in c). The scale bar is 25µm (adapted from [38], with permission of the Optical Society of America).

Currently, AO-OCT is still regarded as basic research tool as only few research grade instruments are available worldwide. Nevertheless, with the help of this technology, fundamental aspects on the anatomy and physiology of the healthy human eye could already be investigated. These included *in vivo* assessment of cone density, RPE cell density, retinal vasculature and the observation of cone renewal, cone function or the disc shedding process. Due to the broader use of other imaging technologies including microscopy (ex vivo) as well as in vivo methods such as AO-SLO or AO fundus camera (which is even commercially available), cell densities have already been measured in a larger population. The aim is to generate a large normative database that allows determining disease related cell packing density changes. However, measurements of these quantities in patients is quite challenging because of the severe changes from the normal retinal structure. The depth sectioning

Biomedical Optics EXPRESS

capabilities of AO-OCT might provide a clear benefit here, as highly scattering structures from other layers that greatly influence these measurements can be excluded.

OCT provides access to the phase of the light returning from the retina. As mentioned above, this can be used to correct for aberrations in post processing. In addition the information enables measuring subtle changes in the optical path length (such as changes of the outer segments length of cones) with high precision [98]. Combining this technology with optical stimulation of the retina provides insights into physiological responses of the retina [119].

All together these aspects will improve our understanding of retinal physiology as these processes can now non-invasively be monitored *in vivo*. This additional information provided by AO-OCT will aid to investigate early stages of a disease and to understand the complex process of disease development. Finally, disease progression can be monitored on a cellular level, which may allow for an earlier assessment of therapeutic success.

However, the development of AO-OCT is still an ongoing process. Advances in technology are likely leading to new insights and new discoveries in retinal function and retinal pathogenesis. In addition the clinical applicability of these instruments will be improved. Since it is unlikely that a large area of the retina is routinely imaged with AO-OCT, standard techniques such as OCT or SLO are required to determine the region of interest. AO-OCT can then be used to provide a detailed view of this region including functional information on the tissue.

In conclusion, we believe that AO-OCT has the potential to play a key role in treatment development, disease diagnosis and even routine screening of the population in order to prevent disease progression at a very early stage of the disease.

Disclosures

MP: Imagine Eyes (F). RJZ: (P)

Funding

Financial support from the Austrian Science Fund (FWF grants P19624-B02 and P22329-N20) and the European Union (European project FAMOS (project number FP7 ICT 317744) is acknowledged. R. J. Zawadzki was supported by the National Eye Institute Grant (R01EY026556), UC Davis Vision Center Core Grant (P30EY012576), UC Davis Research Investments in Science and Engineering (RISE) Grant and NSF I/UCRC CBSS Grants.

Acknowledgments

Michael Pircher likes to thank Chrisoph K. Hitzenberger, Franz Felberer, Matthias Salas, Wolfgang Drexler, Ursula Schmidt-Erfurth and the FAMOS consortium for their collaboration. Robert J. Zawadzki wants to thank his long-term AO-OCT collaborators: John S. Werner, Steven S. Jones, Scott Olivier, Stacey S. Choi, Donald T. Miller, Barry Cense, Ravi S. Jonnal, Marinko V. Sarunic and Yifan Jian.